



City Research Online

City St George's, University of London

Citation: Nazeer, Y. H., Ehmann, M., Koukouvinis, P. & Gavaises, M. (2019). The Influence of geometrical and operational parameters on internal flow characteristics of Internally Mixing Twin-Fluid Y-Jet Atomizers. *Atomization and Sprays*, 29(5), pp. 403-428. doi: 10.1615/atomizspr.2019030944

This is the accepted version of the paper.

This version of the publication may differ from the final published version. To cite this item please consult the publisher's version.

Permanent repository link: <https://openaccess.city.ac.uk/id/eprint/22782/>

Link to published version: <https://doi.org/10.1615/atomizspr.2019030944>

Copyright and Reuse: Copyright and Moral Rights remain with the author(s) and/or copyright holders. Copies of full items can be used for personal research or study, educational, or not-for-profit purposes without prior permission or charge, unless otherwise indicated, provided that the authors, title and full bibliographic details are credited, a hyperlink and/or URL is given for the original metadata page and the content is not changed in any way. For full details of reuse please refer to [City Research Online policy](#).

The Influence of geometrical and operational parameters on internal flow characteristics of Internally Mixing Twin-Fluid Y-Jet Atomizers

Y. H. Nazeer^{1*}, M. Ehmann¹, P.Koukouvini², M. Gavaises²

¹Mitsubishi Hitachi Power Systems Europe GmbH, Germany

² School of Mathematics, Computer Sciences and Engineering, City University of London, UK

DOI: [10.1615/AtomizSpr.2019030944](https://doi.org/10.1615/AtomizSpr.2019030944)

Keywords: Internally Mixing Twin-Fluid Y-Jet Atomizer, Compressible Volume of Fluid (VOF), Large Eddy Simulations (LES), Multiphase Flow Regimes.

Abstract

Internally mixing twin-fluid Y-jet atomizers are widely used in coal fired thermal power plants for start-up, oil-fired thermal power plants and industrial boilers. The flow through internally mixing Y-jet atomizers is numerically modeled using the compressible Navier-Stokes equations; Wall Modeled Large Eddy Simulations (WMLES) is used to resolve the turbulence with Large Eddy Simulations whereas the Prandtl Mixing Length Model is used for modeling the subgrid scale structures, which are affected by geometric and operational parameters. Moreover, the Volume-of-Fluid (VOF) method is used to capture the development and fragmentation of the liquid-gas interface within the Y-jet atomizer. The numerical results are compared with correlations available in open literature for the pressure drop; further results are presented for the multiphase flow regime maps available for vertical pipes. The results show that the mixing point pressure is strongly dependent on the mixing port diameter to airport diameter ratio, specifically for gas to liquid mass flowrate ratio (GLR) in the range $0.1 < \text{GLR} < 0.4$; the mixing port length moderately affects the mixing point pressure while the angle between mixing and liquid ports is found not to have an appreciable effect. Moreover, it is found that the vertical pipe multiphase flow regime maps in the literature could be applied to the flow through the mixing port of the twin-fluid Y-jet atomizer. The main flow regimes found under the studied operational conditions are annular and wispy annular flow.

Introduction

Twin-fluid atomizers have been used in numerous industrial applications over the years such as gas turbines (Lefebvre, 1988), internal combustion engines (Wade, et al., 1999), spray drying (Mujumdar, et al., 2010), spray coating (Esfarjani & Dolatabadi, 2009), scramjet engines (Gadgil & Raghunandan, 2011),

- 32 fire suppression (Huang, et al., 2011), process industries (Loebker & Empie, 1997) and power plants
 33 (Zhou, et al., 2010). They use compressed air or steam to

Nomenclature

Acronyms

SMD	Sauter Mean Diameter
VOF	Volume of Fluid
WMLES	Wall Modeled Large Eddy Simulations
LES	Large Eddy Simulations
RANS	Reynolds-Averaged Navier-Stokes
GLR	Gas to Liquid Mass Flow Rate Ratio
SGS	Subgrid Scale
Eq.	Equation
Noz.	Nozzle

Subscripts

p	Phase p
q	Phase q
m	Mixing Point
a	Air
G	Gas
l	Liquid
i, j, k	Direction Vector
1,2	Points Along the Length of Mixing-Port
max	Maximum
min	Minimum

Superscript

T	Transpose
s	Sub-grid Scale

Symbols

α	Volume Fraction
ρ	Density, kg/m^3
V	Velocity, m/s
P	Pressure, Pa
μ	Viscosity, $kg/m \cdot s$
g	Gravitational Acceleration, m/s^2
T_σ	Surface Tension Force, N
T	Temperature, K
k	Curvature, m^{-1}
σ	Surface Tension, N/m
E	Energy, J
K_{eff}	Effective Thermal Conductivity, $W/m \cdot K$
Δ	Modified Length Scale, m
τ	Reynold Stress Tensor, N/m^2
ν_t	Eddy Viscosity, m^2/s
δ	Kronecker Delta
y^+	Dimensionless Wall Distance
Ω	Vorticity, s^{-1}

S	Strain Rate, s^{-1}
θ	Angle, $^{\circ}$
l	Length, mm
d	Diameter, m
$\bar{\tau}$	Viscous Stress Tensor, kg/ms^2
φ	Momentum Ratio
V_r	Relative Velocity, m/s
We	Weber Number
Z	Coordinate Along the Length of Mixing-Port
\dot{m}	Mass Flow Rate, kg/s
G	Mass Velocity, kg/m^2s
J	Superficial Velocity, m/s
Fr_{tp}	Two Phase Froude Number
Q	Volume Flow Rate, m^3
c	Speed of Sound, m/s
R	Radius, m
μ'_l	Ratio of Liquid Viscosity to Water Viscosity at Standard Conditions
ρ'_l	Ratio of Liquid Density to Water Density at Standard Conditions
σ'_l	Ratio of Liquid Surface Tension to Water Surface Tension at Standard Conditions
A	Parameter Defined in Eq. 19
C_w	Empirical Constant
h_{max}	Maximum Edge Length, m
h_{wn}	Grid Step in Wall Normal Direction, m
d_w	Distance from Wall, m
C_{smag}	Smagorinsky Constant

34 augment the atomization process; they are classified into internally and externally mixing twin-fluid
35 atomizers. In externally mixing atomizers, high velocity gas or steam impinges on the liquid just outside
36 the discharge orifice, while in internally-mixing ones, the gas or steam mixes with the liquid inside the
37 nozzle before being injected. In the internal mixing type, the spray cone angle is minimum for maximum
38 gas flow while the spray widens as gas flow reduces. This type of atomizer is well suited for high viscous
39 liquids as good atomization could be obtained at low liquid flow rates (Barreras, et al., 2008). It is far
40 more efficient than the externally mixing concept as lower gas flow rates are needed to achieve the
41 same degree of atomization (Tanasawa, et al., 1978). However external mixing atomizers have the
42 advantage of producing sprays with constant spray angle at all liquid flow rates independently of the
43 back pressure, as there is no communication between the flowing media internally.

44 Undoubtedly, there are various ways to generate the atomized sprays using various types of nozzles,
45 including for example rotary cups (Nguyen & Rhodes, 1998), twin-fluids (Lefebvre, 1988), (Wade, et al.,
46 1999), (Li, et al., 2018), (Mujumdar, et al., 2010), (Esfarjani & Dolatabadi, 2009), (Gadgil & Raghunandan,
47 2011), (Huang, et al., 2011), (Loebker & Empie, 1997) and (Zhou, et al., 2010), pressure swirl (Radcliffe,
48 1955), (Dafsari, et al., 2017) and (Arcoumanis & Gavaises, 1999), fan (Dombrowski, et al., 1960),

49 ultrasonic (Lang, 1962), electrostatic (Maski & Durairaj, 2010), diesel injectors (Arcoumanis, et al., 1999)
50 and (Mitroglou & Gavaises, 2011) and effervescent atomizers (Sovani, et al., 2001) and (Saleh, et al.,
51 2018); solid or hollow cone sprays may form depending on the type of atomizer and operating
52 conditions. However, in thermal power plants or oil-fired large industrial boilers, operating with high
53 flow rates of viscous fuel, mostly Y-jet or internal mixing chamber twin-fluid atomizers are used
54 (Barreras, et al., 2006). The former is used with light and medium fuel oil while the latter is used with
55 heavy fuel oil (Li, et al., 2012), with steam as auxiliary fluid. An obvious advantage of using the steam is
56 that any heat transfer from the steam to the fuel in the mixing port will enhance atomization by
57 reducing the fuel's viscosity and surface tension. In contrast, the comparative test carried by (Bryce, et
58 al., 1978) showed that compressed air produced much finer spray than steam. (Barreras, et al.,
59 2006)[20] demonstrated that for the same liquid mass flow rate, the internal mixing chamber twin-fluid
60 atomizer requires a lower atomizing fluid mass flow rate than an equivalent Y-jet one, simultaneously
61 yielding droplets with smaller Sauter Mean Diameter. The characteristic of the Y-jet atomizer is that
62 liquid and gas (steam or air) is mixed before injected out. It generally consists of a number of jets from
63 minimum of 2 to maximum of 20, arranged in an annular manner to provide hollow conical spray. The
64 advantage of such an atomizer is that it could be operated by keeping constant gas-to-liquid mass flow
65 rate ratio; and the requirement of the atomizing fluid is low. Y-jet atomizers are reported to maintain
66 moderate emission rate while attaining relatively high atomization efficiency (Pacifico & Yanagihara,
67 2014). This kind of atomizers create high relative velocity by injecting gas at high velocity, which induces
68 disturbances in the liquid jet and leads to the creation of smaller liquid ligaments; subsequently, smaller
69 droplets are formed due to ligament's breakup due to aerodynamically-induced surface waves
70 (Dombrowski & Johns, 1963). The high relative velocity of the gas helps dispersion of the liquid and
71 prevents droplets coalescence (Pacifico & Yanagihara, 2014).

72 Twin-fluid atomizers have been studied extensively over the years. Most of the studies are focused on
73 pre-filming air blast atomizers or effervescent atomizers due to their extensive commercial use. The
74 earlier are used extensively in aircraft, marine and industrial gas turbines and the latter are used in
75 various applications where low injection pressures and low gas flow rates are available. There exist
76 considerable studies on internally mixing twin-fluid Y-jet atomizers. However, the understanding of such
77 nozzle is not very clear owing to complex aerodynamic and fluid dynamic flow pattern due to the mixing
78 of gas and liquid within the mixing chamber.

79 Mullinger and Chigier (Mullinger & Chigier, 1974) were the first to study the performance of such
80 atomizer systematically. According to them, and as shown pictorially by Song & Lee (Song & Lee, 1996),
81 some atomization occurs within the mixing chamber, but most of the liquid emanates from the atomizer
82 in the form of liquid that is then shattered into droplets by the atomizing fluid. (Mullinger & Chigier,
83 1974) and (Prasad, 1982) reported an extensive parametric study and proposed design criteria for the Y-
84 jet twin-fluid nozzles. In fact, the results of Mullinger and Chigier showed good agreement with the
85 empirical dimensionless correlation of mass median diameter for air-blast atomizer proposed by Wigg
86 (Wigg, 1959). It is pertinent to mention here that the choice to name an atomizer as air-assist or air-
87 blast atomizer is arbitrary. Usually, air-assist atomizers employ very high velocities that usually
88 necessitate an external supply of high pressure steam/air, while lower gas requirement of air-blast
89 atomizers can usually be met by utilizing the pressure differential across the combustion liner.

90 Andressui et al (Andreussi, et al., 1992) reported that the length to diameter ratio of the mixing port
91 influences the pressure drop, spray structure and droplet size distribution based on a semi-empirical
92 model of the flow inside twin-fluid Y-jet atomizer. Song and Lee (Song & Lee, 1994) studied the effect of
93 the mixing port length and the injection pressure on the flowrates of the gas and liquid and droplet size
94 distribution. Andreussi et al (Andreussi, et al., 1994) explained the internal flow conditions and the liquid
95 film thickness inside the mixing duct and postulated their effect on external spray characteristics. Song
96 and Lee (Song & Lee, 1996) made a pictorial study of the internal flow pattern of Y-jet atomizer and
97 described the internal flow as annular / annular mist flow (Chin & Lefebvre, 1993); they proposed the
98 main mechanism involved in fuel atomization and linked the internal flow pattern to the droplet size
99 distribution in the spray. Mlkvik et al (Mlkvik, et al., 2015) compared the performance of four different
100 internally mixing twin-fluid atomizers for the range of different operating conditions and liquid
101 properties. They found that the internally mixing Y-jet atomizer to produce most stable spray regardless
102 of pressure differential and gas to liquid ratio (GLR). The internal flow pattern for the Y-jet atomizer
103 showed strong agreement with the results of Song & Lee (Song & Lee, 1996) and Nazeer et al. (Nazeer,
104 et al., 2018).

105 Ferreira et al (Ferreria, et al., 2009) demonstrated that under certain experimental conditions the
106 atomizing fluid flow is choked in internally mixing chamber twin-fluid atomizer. Sonic conditions are
107 achieved at different mass flow rates as a function both of the air/gas channel diameter and liquid mass
108 flow rate. They found that under choked conditions there is a certain channel diameter that produced
109 smallest Saunter Mean Diameters (SMD).

110 There are two different ways in which two-phase flow are commonly represented in CFD, namely the
111 “Eulerian” method, where the flow is considered as continuous across the whole flow domain and the
112 “Lagrangian” method, where the paths taken by the particles/droplets are tracked through the domain
113 (Jang, et al., 2010). In the Lagrangian particle tracking approach, the gas phase is still represented using
114 an Eulerian approach by solving the governing equations of the flow but the liquid spray is represented
115 by a number of discrete “computational particles”, which are tracked by solving the particle’s equation
116 of the motion. The fundamental assumption made in this approach is that the dispersed secondary
117 phase occupies a low volume fraction (typically below 10%) (El-Batsh, et al., 2012). Therefore, this
118 approach is not appropriate to model the multiphase flow within the nozzle where the volumetric effect
119 of the secondary phase cannot be neglected. Eulerian methods could be further classified into single-
120 fluid, such as relevant mixture and VOF models, and multi-fluid approaches like Eulerian multiphase and
121 multi-fluid VOF models (Crowe, 2006) and (Loth, 2009). The latter approach treats each phase as a single
122 independent phase but intermixed continua while the earlier treats the flow as a single-phase flow by
123 solving a single set of conservation equations considering the mixture properties. The single fluid
124 approach assumes that the continuous and the dispersed phases are in local kinetic and thermal
125 equilibrium, i.e. the relative velocities and temperatures between the two phases are small in
126 comparison to predicted variations of the overall flow field (Lakhehal, et al., 2002). The multi-fluid
127 approach requires separate conservation equation for each phase, making it extremely computational
128 expensive and complex; hence, this rules out the possibility of utilizing it for extensive parametric
129 studies. On the other hand, the mixture model solves a smaller number of equations as compared to the
130 aforementioned models; however, it is not possible to track the interface between the phases. This is
131 major drawback for the studies aiming to identify the relevant flow regimes. The Eulerian surface
132 tracking technique i.e. the VOF method can track with relatively good accuracy the interface between
133 the phases; this makes it feasible to study the in-nozzle flow and primary break-up of the jets (Gopala &
134 Berend, 2008). Hence it is considered to be a viable option to model the multiphase flow through Y-jet
135 atomizer.

136 Scale resolving technique i.e. Large Eddy Simulations (LES) can simulate turbulent flows since 1960s. It
137 has made significant progress over last two decades specifically due to surge in computing power. The
138 hybrid LES technique is beginning to emerge as a viable alternative to time-averaged or ensemble-
139 averaged Navier-Stokes (RANS) turbulence modeling in industrial flows; it is able to capture flow
140 structures larger than the grid size, while smaller scales are modeled with subgrid scale models (SGS).
141 The spectrum of resolved scales in LES is directly dependent on the grid resolution. This makes it

142 extremely expensive for industrial scale simulations, which are usually highly turbulent, wall bounded,
143 viscous and three dimensional flows. Nevertheless, Wall Modeled LES (WMLES) is a substitute to
144 classical LES and it reduces the stringent and Reynold number dependent grid resolution requirements
145 of classical wall-resolved LES. Turbulence length scales in near-wall regions are directly proportional to
146 wall distance, resulting in smaller and smaller eddies as the wall is approached (Naseri, et al., 2018). This
147 effect is limited by molecular viscosity, which damps out eddies inside the viscous sublayer. Smaller
148 eddies appear as the Reynold number increases, since the viscous sublayer becomes thinner. In order to
149 circumvent the resolution of these small near-wall scales, RANS and LES models are combined such that
150 the RANS model covers the very near-wall layer, in which the wall distance is much smaller than
151 boundary layer thickness but is still potentially very large in wall units (Piomelli & Balaras, 2002). It then
152 switches over to the LES formulation once the grid spacing becomes sufficient to resolve the local scales
153 (Wen & Piomelli, 2016). This approach is similar to detached eddy simulations (Spalart, et al., 1997) and
154 delayed detached eddy simulations (Spalart, et al., 2006) and (Koukouvinis, et al., 2016). A general
155 approach of these two approaches is that the whole or major part of the boundary layer is modeled by
156 RANS while LES is applied only to separated flow regions. In contrast, as aforementioned, in WMLES,
157 RANS is used only in very thinner near wall region (Koukouvinis, et al., 2016).

158 There is a dearth of numerical studies on internally mixing twin-fluid Y-jet atomizers, probably owing to
159 complexity involved in modeling the complex multi-phase flow pattern due to variations in length and
160 time scales. However, there exists few numerical studies such as (Tanner, et al., 2016) focusing on the
161 atomization and droplet break up in annular gas-liquid co-flow for internally mixing twin-fluid Y-jet
162 atomizer, (Tapia & Chavez, 2002) focusing on the internal flow pattern. In all studies except (Song & Lee,
163 1996), (Andreussi, et al., 1994), (Mlkvik, et al., 2015), (Pacifico & Yanagihara, 2014) and (Tapia & Chavez,
164 2002), the parameters such as injection conditions and atomizer geometry were taken as input while the
165 spray dispersion was the reported output. But the intermediate process between the input and output
166 of the nozzle has not been investigated in detail.

167 The present paper is the first to numerically model the multiphase flow through twin-fluid Y-jet
168 atomizer as function of the various operating conditions affecting it. In (Nazeer, et al., 2018) the authors
169 have utilized the same computational model as in the present study and concluded on the influence of
170 momentum ratio and gas to liquid ratio (GLR) on the internal flow development for a specific geometry.
171 In the present study, the analysis extents to the effect of geometric parameters of Y-jet atomizers. The

172 presented results are used for validation of the developed model against relative literature findings for
 173 the pressure drop and the complex flow regime charts available in the literature for such nozzles.

174 Numerical Method

175 The compressible Navier-Stokes equations are employed using the finite volume approximation; the
 176 Volume of Fluid (VOF) technique with Geometric Reconstruction Scheme is employed in ANSYS Fluent to
 177 model the gas-liquid interface. The phases in bulk are treated as non-interpenetrating continua, i.e. in
 178 most of the cells the volume fraction is either one or zero. The interface is modeled as interpenetrating
 179 i.e. volume fraction in any cell could be between 0 and 1.

180 Interface is tracked with the following continuity equation. Here α_q is volume fraction in the cell, ρ_q is
 181 the density and \vec{V}_q is the velocity vector of q^{th} phase.

$$\frac{d}{dt}(\alpha_q \rho_q) + \nabla \cdot (\alpha_q \rho_q \vec{V}_q) = 0 \quad (1)$$

182
 183 The single set of momentum equation is shared among the phases based on mixture properties.

$$\frac{d}{dt}(\rho \vec{V}) + \nabla \cdot (\rho \vec{V} \vec{V}) = -\nabla P + \nabla \cdot [\mu(\nabla \vec{V} + \nabla \vec{V}^T)] + \rho \vec{g} + \vec{T}_\sigma \quad (2)$$

184
 185 Where density is defined as: $\rho = \sum \alpha_q \rho_q$, viscosity as: $\mu = \sum \mu_q \alpha_q$, and velocity as: $\vec{V} = \frac{1}{\rho} \sum_{q=1}^n \alpha_q \rho_q \vec{V}_q$
 186 \vec{T}_σ is the volumetric force source term arising due to the surface tension. It is modelled by continuum
 187 surface force model proposed by Brackbill et al (Brackbill, et al., 1992). This model treats the surface
 188 tension as the pressure jump across the interface. The forces at the surface are expressed as volume
 189 forces using divergence theorem.

$$T_\sigma = \sum_{pairs, p, q} \sigma_{p, q} \frac{\alpha_p \rho_p k_q \nabla \alpha_q + \alpha_q \rho_q k_p \nabla \alpha_p}{\frac{1}{2}(\rho_p + \rho_q)} \quad (3)$$

190
 191 The curvature of one surface is negative of other, $k_p = -k_q$ and divergence of the volume fraction is
 192 negative of other $\nabla \alpha_p = -\nabla \alpha_q$. This simplifies the equation to:

$$T_\sigma = \sigma_{p, q} \frac{\rho k_p \nabla \alpha_p}{\frac{1}{2}(\rho_p + \rho_q)} \quad (4)$$

193 The total energy of the flow is modelled by following equation.

$$\frac{d}{dt}(\rho E) + \nabla \cdot (\vec{V}(\rho E + P)) = \nabla \cdot (K_{eff} \nabla T + \bar{\tau} \cdot \vec{V}) \quad (5)$$

194

195 Here K_{eff} is effective thermal conductivity, $\bar{\tau}$ is the viscous stress tensor; the energy E and temperature
196 T are mass averaged variables.

$$E = \frac{\sum_{q=1}^n \alpha_q \rho_q E_q}{\sum_{q=1}^n \alpha_q \rho_q} \quad (6)$$

197

198 E_q is the internal energy of each phase; both phases share the same temperature.

199 Scale resolving technique is adopted to resolve larger eddies through Wall Modeled LES (WMLES) Model.

200 As Reynolds number increases and the boundary layer become thinner, the size of important energy

201 bearing eddies decreases. In LES, the important energy bearing eddies must be resolved, thus the cost of

202 maintaining grid resolution becomes prohibitive. In this model larger eddies are resolved while eddies in

203 thinner near-wall regions; in which the wall distance is much smaller than boundary-layer thickness but

204 is still potentially very large in wall units (Piomelli & Balaras, 2002), is modeled with RANS, hence

205 considerably reducing the computational cost. Gaussian filter is applied to filter out eddies based on

206 length scale Δ (Shur, et al., 2008).

$$\bar{\phi}(x, t) = \int_D \phi(x', t) G(x, x', \Delta) dx' \quad (7)$$

$$\Delta = \min(\max(C_w \cdot ds_w; C_w \cdot h_{max}, h_{wn}); h_{max}) \quad (8)$$

207

208 h_{max} = maximum edge length, h_{wn} = grid step in wall-normal direction, $C_w=0.15$, d_w = distance from wall.

209 After putting the filtered out variables in Navier-Stokes equation and rearranging the terms, it could be

210 expressed as:

$$\frac{\partial \bar{V}_i}{\partial t} + \frac{\partial (p \bar{V}_i \bar{V}_j)}{\partial x_j} = -\frac{\partial \bar{P}}{\partial x_i} + \frac{\partial (\bar{\tau}_{ij} + \tau_{ij}^s)}{\partial x_j} \quad (9)$$

211 This equation could be resolved except subgrid-scale stress τ_{ij}^s . It can be expressed by the

212 Boussinesq hypothesis (Hinze, 1975) as:

$$\tau_{ij}^s - \frac{1}{3} \tau_{kk} \delta_{ij} = -2\mu_t S_{ij} \quad (10)$$

213 The subgrid scale eddy viscosity is modeled with Smagorinsky SGS model (Smagorinsky, 1963) with van
 214 Driest damping (Van Driest, 1956) and mixing length model as:

$$\nu_t = \min \left[(kds_w)^2, (C_{smag}\Delta)^2 \right] \left[1 - \exp[-(y^+/25)^3] \right] |S - \Omega| \quad (11)$$

215 $C_{smag} = 0.2$ is the Smagorinsky constant, as established by Shur et al (Shur, et al., 1999), $\Omega=$ is the
 216 vorticity, S is the magnitude of the strain tensor, $k = 0.41$ is the Von Karman Constant.

217 Test Case Simulated

218 Seven different Y-jet atomizers are used for the parametric analysis. Air and water are used as working
 219 fluids at atmospheric conditions. The geometries are constructed in ANSYS Design Modeler according to
 220 the design criteria of Mullinger & Chigier (Mullinger & Chigier, 1974); the same design criteria were also
 221 adopted by Pacifico & Yanagihara (Pacifico & Yanagihara, 2014) for the experimental study on pressure
 222 drop within internally mixing twin-fluid Y-jet atomizers. The geometries are meshed in ANSYS Meshing
 223 tool. The grids are polyhedral with the number of elements ranging between 15 to 17.3 million. The Y^+
 224 values are in the range of 0.72 - 0.94. The schematic of the nozzle studied is shown in Figure 1. Table 1
 225 shows the geometrical parameters of all the seven atomizers. All the pressure points as shown in the
 226 Figure 1 i.e. P_a , P_w , P_m , P_1 and P_2 are obtained from the numerical solutions, where P_m is the mixing
 227 point pressure, P_a is the gas (air) inlet pressure, P_w is the liquid (water) inlet pressure, P_1 is the pressure
 228 at the middle point along the length of mixing port and P_2 is the pressure near the exit of the mixing
 229 port. Mass flow boundary conditions are employed at the gas port and liquid port inlets while pressure
 230 outlet boundary condition is employed at the exit of the mixing duct.

231 In order to keep geometrical and operational similarity with the work of Pacifico & Yanagihara (Pacifico
 232 & Yanagihara, 2014), non dimensionless number i.e. Weber numbers are calculated for the flow in the
 233 mixing duct. Weber numbers used by Pacifico & Yanagihara (Pacifico & Yanagihara, 2014) are in the
 234 range of 500 – 42500, while the Weber numbers used in this work are also nearly in the same range i.e.
 235 between 600 – 45000. Weber numbers are calculated with the following formula:

$$We = \frac{\rho_{a,m} V_r^2 d_m}{\sigma} \quad (12)$$

236 Where $\rho_{a,m}$ is the density of the air at the mixing point, V_r is the relative velocity between the air and
 237 water, d_m is the mixing port diameter. The mass flow rate of air and water were also applied almost in

238 the same range as stated in the literature. The mass flow rate of the air was in the range 0.008 kg/s to
 239 0.091 kg/s while mass flow rate of the water was in the range 0.075 kg/s to 0.78 kg/s.

240 For each of the seven nozzles a total of 11 simulations were performed. Gas to liquid mass flow rate
 241 ratio (GLR) was varied from 0.01 to 0.9. The main geometrical parameters studied includes: the angle (θ)
 242 between liquid port and the mixing port; mixing port length to diameter ratio (l_m/d_m) and mixing port
 243 diameter to gas port diameter ratio (d_m/d_g). The values used for the aforementioned geometrical
 244 parameters are in the range: $\pi/4 \leq \theta \leq 7\pi/18$ ($45^\circ - 70^\circ$); $3.5 \leq l_m/d_m \leq 10$ and $1.67 \leq$
 245 $d_m/d_g \leq 2$. The following sets of atomizers were used for each of the parametric study: nozzles B, D
 246 and E are used for the parametric study of θ ; B, F and G for l_m/d_m and A, B and C for d_m/d_g . These
 247 values are shown in the Table 1 for each nozzle.

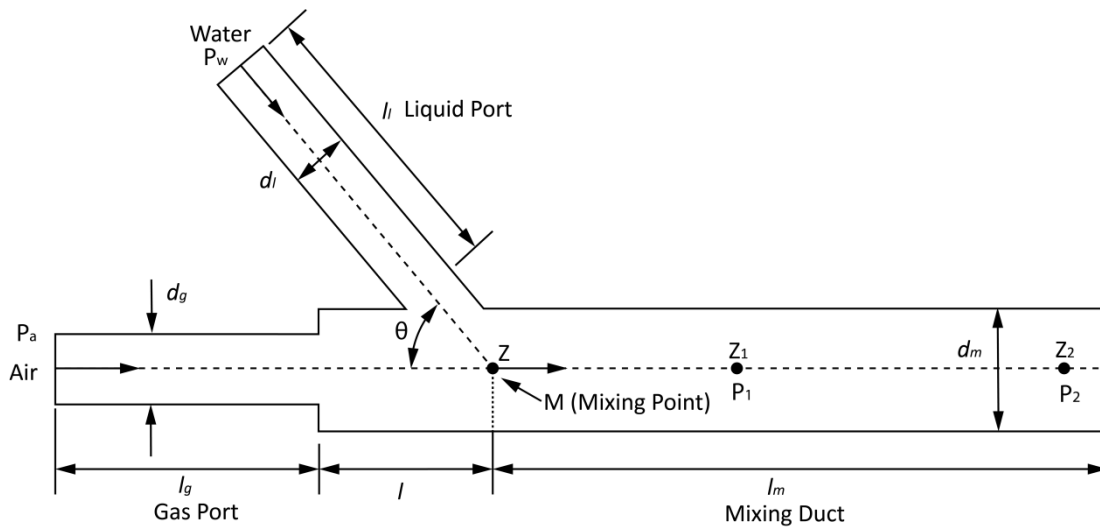


Figure 1: Schematic of the nozzle used for the parametric study.

Table 1: Geometric values for the parameters shown in Fig. 1.

Nozzle	l_g (mm)	l (mm)	l_m (mm)	d_g (mm)	d_m (mm)	θ	l_m/d_m	d_m/d_g	z_1 (mm)	z_2 (mm)
A	50	14.4	50	5.5	10	57°	5.00	1.82	25	42.5
B	50	14.4	50	6.0	10	57°	5.00	1.67	25	42.5
C	50	14.4	50	6.0	12	57°	4.17	2.00	25	42.5
D	50	16.2	50	6.0	10	45°	5.00	1.67	25	42.5
E	50	13.0	50	6.0	10	70°	5.00	1.67	25	42.5
F	50	14.4	35	6.0	10	57°	3.50	1.67	17.5	27.5
G	50	14.4	100	6.0	10	57°	10.00	1.67	50	92.5

257

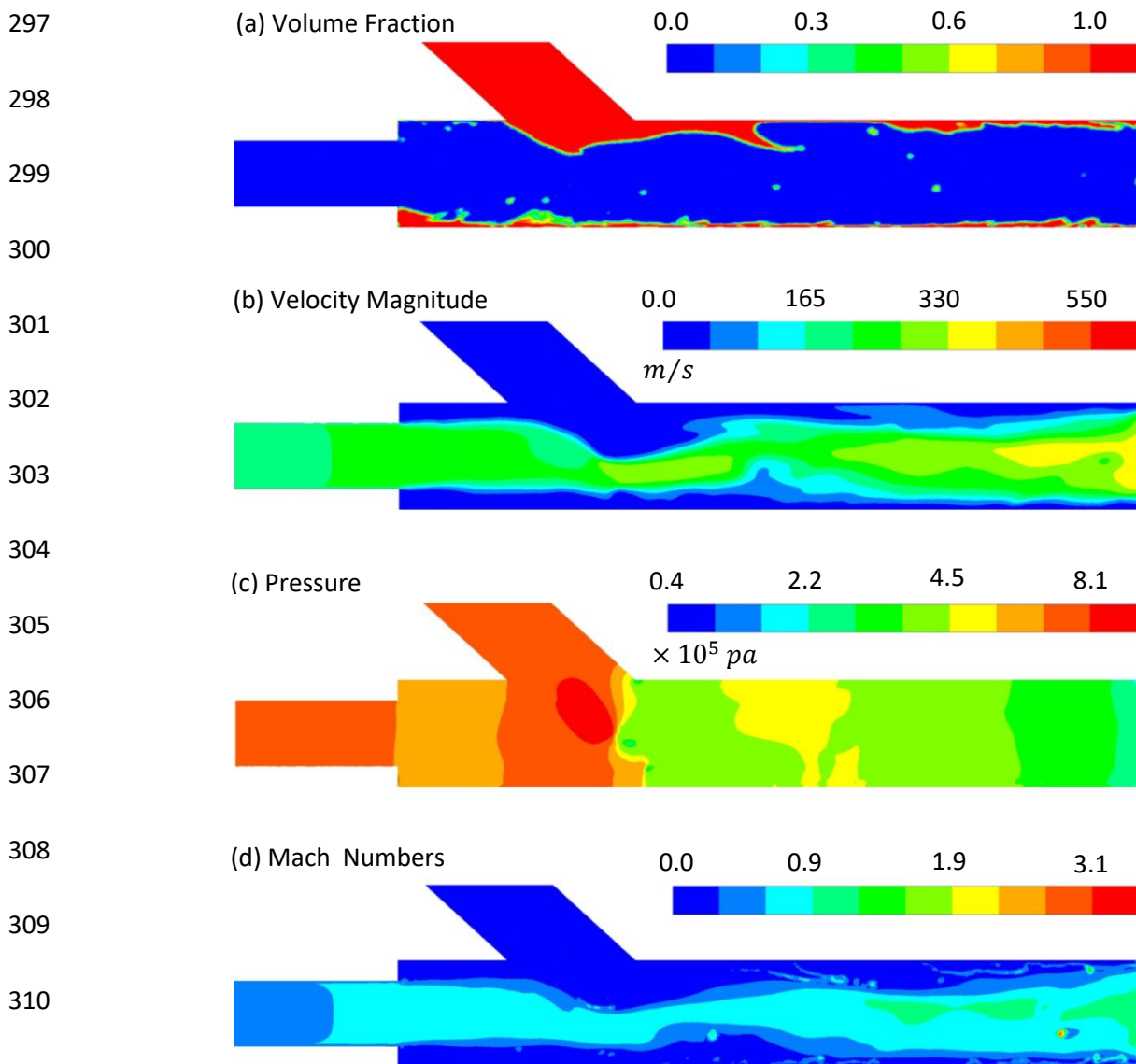
258

259 **Results and Discussion**

260 Figure 2a shows contours of the volume fraction of water and air. At first it could be seen that the gas-
261 liquid flow is annular, with the liquid film formed on the inner wall of the mixing duct. As the high speed
262 air jet impinges on the liquid jet, it creates disturbance on the surface of the liquid column; leading to
263 creation of wavy structure in the liquid column/film. This may lead to inception of the primary breakup
264 of the liquid jet within the nozzle. The liquid film formed just downstream of the gas port in the mixing
265 duct is because of the recirculation of the air due to its expansion from the gas port into the mixing duct.
266 The expansion of the air is limited by the higher pressure of the liquid jet (Figure 2c). This leads to
267 recirculation of the air in the pre-mixing zone of the mixing duct. Figure 3a shows the recirculating
268 velocity vectors in the recirculating zone. Figure 3b is the schematic illustration of the reverse flow and
269 liquid film formation in the premixed zone. A portion of the water stream is flowed backward in the
270 form of film towards the upstream by the recirculating air flow. When the reverse film flow meets the
271 main air stream at the exit of the gas port, it disintegrates into droplets and flows downstream along the
272 core, as illustrated in Figure 3b. Figure 2b shows the contour of the velocity. Air jet accelerates as it
273 expands from the gas port in to the mixing duct. It further accelerates as it bypasses the relatively slow
274 moving liquid jet emanating from the liquid port. It then slightly decelerates while aligning with the
275 liquid film before it rapidly accelerates towards the exit of the nozzle. Figure 2c is the contour of the
276 pressure. The higher pressure around the area of air impingement on the liquid column is due to the
277 increase in static pressure because of dynamic pressure of the air jet. Figure 2d shows the contour of the
278 Mach number of the forming multi-phase flow. The speed of the sound is much lower in the gas-liquid
279 mixture than in either pure liquid or gas component. For example, it is 1480 m/s in water and 340 m/s in
280 air, but in air-water mixture it can fall to 20 m/s (McWilliam & Duggins, 1969). This process occurs
281 because the two-phase system has the effective density of the liquid but the compressibility of the gas
282 (Kieffer, 1977) (refer to appendix A for further details). In Figure 2d it can be seen that in the mixing duct,
283 Mach numbers are higher at the gas liquid interface and around the exit of the nozzle. Although the
284 instantaneous Mach numbers could be higher than one, there is no evidence of flow choking in the
285 mixing duct. Pacifico & Yanagihara (Pacifico & Yanagihara, 2014) also reached to the same conclusion
286 about gas-liquid multiphase flow in the mixing duct of Y-Jet atomizer.

287 Figure 4 and Figure 5 depicts the plots of the ratios of mixing point pressure to air inlet pressure (P_m/P_a)
288 and water inlet pressure to air inlet pressure (P_w/P_a) against the GLR ratios respectively. At first, in
289 qualitative terms the results of all the nozzles are similar i.e. with increasing GLR both ratios decrease.

290 Increase in GLR is attributed to either increase in air mass flow rate or decrease in water mass flow rate.
291 This, in turn, induces the air flow momentum to have larger influence on the mixing process and
292 particularly on mixing point pressure. On the other hand, water flow determines the back pressure for
293 the air jet expanding from the gas port into the mixing port. This behavior is inherent to any
294 compressible flow expansion. It could be seen that rate of decrease of P_w/P_a ratio is higher than that of
295 P_m/P_a ratio. This is because the water mass flow rate limits the expansion of the gas stream and hence
296 leads to the conclusion that P_m among the others are controlled by the water inlet pressure.



312 **Figure 2: Flow field for the nozzle D with GLR =0.29 (a) volume fraction contours, (b) velocity contour, (c)**
313 **pressure contour and (d) Mach number contour.**

314
315
316
317
318
319
320
321
322
323
324
325
326
327
328
329
330
331
332
333
334
335
336
337
338
339
340

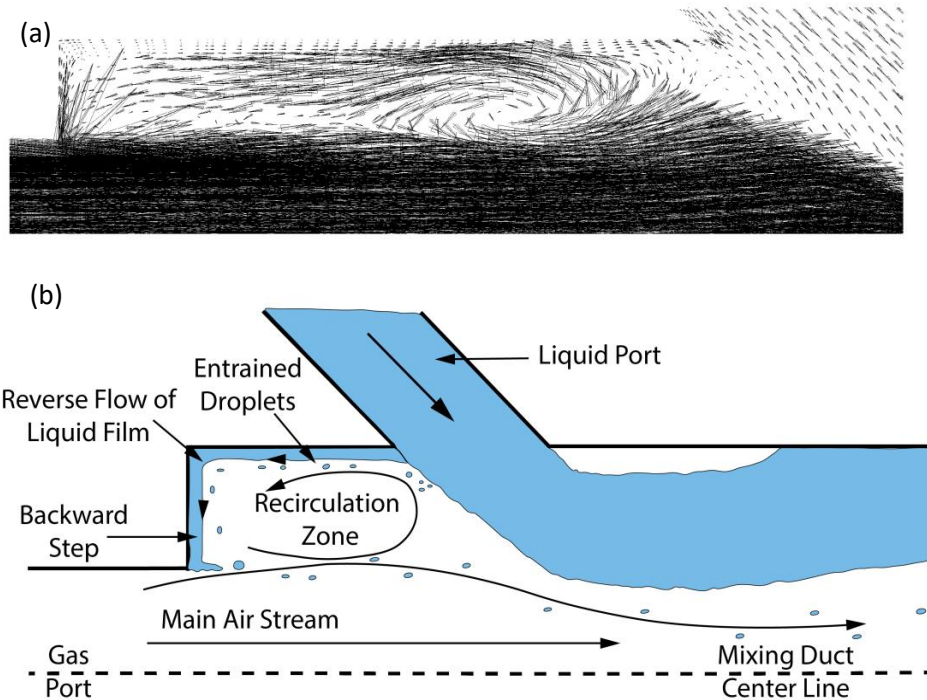
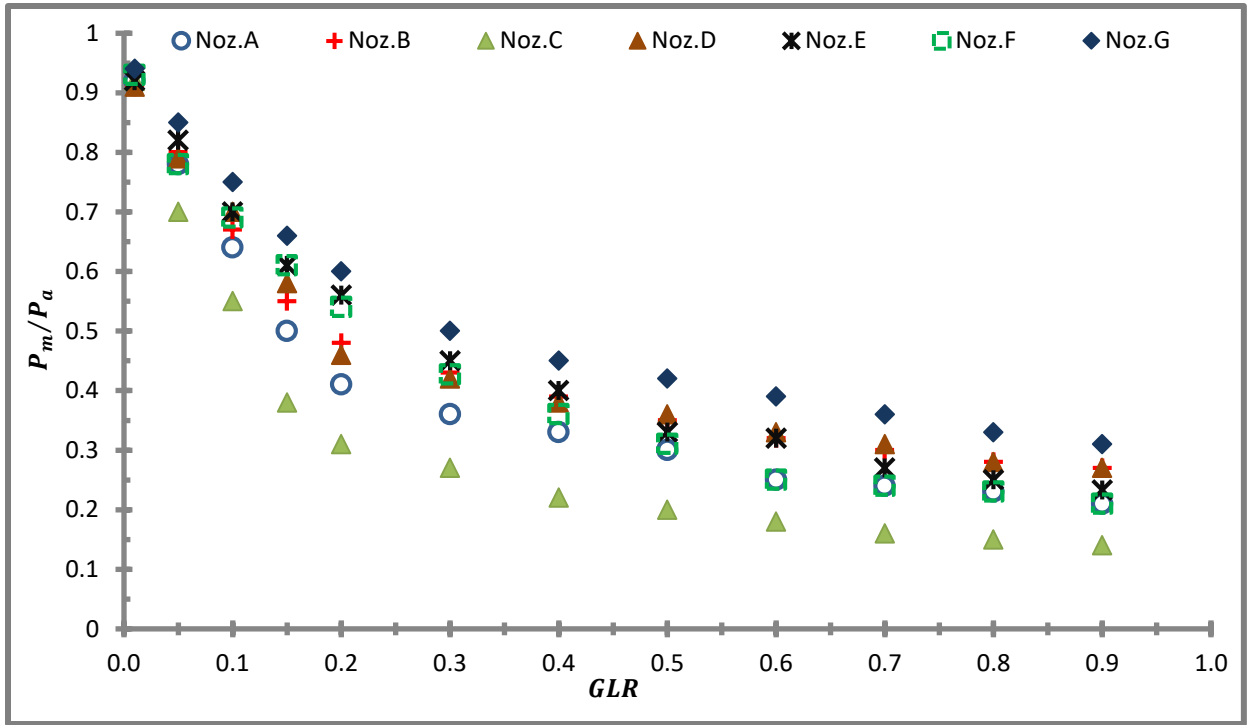


Figure 3: (A) recirculating velocity vectors in recirculation zone, (B) schematic illustration of recirculating air flow and reverse film formation.

It could be seen from the plots that except for $GLR = 2$, there is virtually no difference among the results obtained for the angle between the mixing port and the liquid port as the function of GLR (nozzle B, D and E). This concludes that the angle doesn't have significant effect on the mixing point pressure. Ferreira et al (Ferreira, et al., 2009) reached to the same conclusion for the effect of angle on the Saunter Mean Diameter (SMD) of the droplets produced by twin-fluid atomizer with the mixing chamber. This leads to the hypothesis that the mixing point pressure does plays a role in the performance of internally mixing twin-fluid atomizer. Regarding the influence of l_m/d_m ratio on the mixing point pressure (Nozzles B, F and G), it could be noticed that the mixing point pressure increases with the increasing l_m/d_m ratio. It should be noted that d_m is constant for all the three nozzles; hence the mixing point pressure increases with increasing mixing port length. This behavior is explained due to the smoother drop of the pressure for the large values of l_m . Since the outlet pressure is the same for all the nozzles (i.e. atmospheric pressure), the nozzle with higher value of l_m has higher P_m . Mullinger & Chigier (Mullinger & Chigier, 1974) reported that droplet size decreases for the nozzle with longer mixing port while in contrast Song and Lee (Song & Lee, 1994) reported that droplet size decreases with shorter mixing port length. This contradiction was latter clarified by Song and Lee (Song & Lee, 1996). They reported that for relatively small liquid mass flow rate and high gas flow rate, the droplets generated by the nozzle with shorter mixing port are generally smaller than the droplets generated by

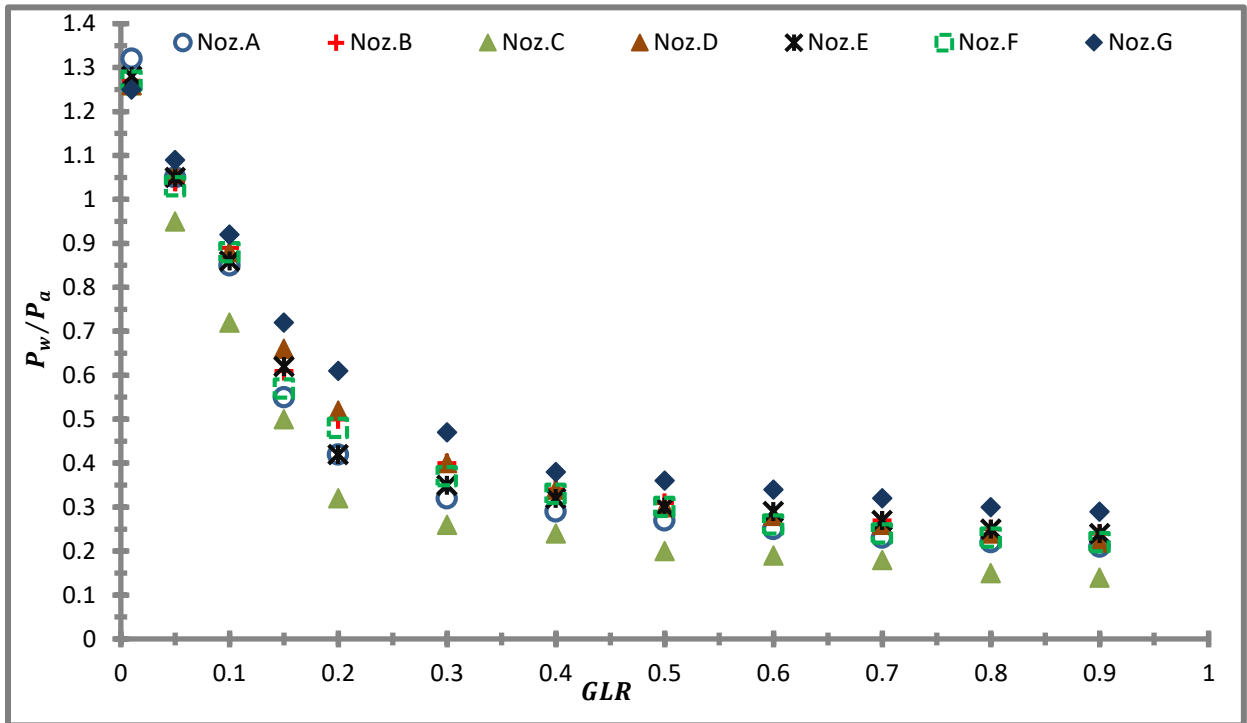
341 the nozzle with longer mixing port; whereas for relatively large liquid mass flow rate and smaller gas
342 flow rate, the droplets produced by the nozzle with longer mixing port are comparable or even slightly
343 smaller than the drops produced by nozzle with smaller mixing port length. This discrepancy could be
344 explained with the work of Lefebvre (Lefebvre, 1992). At low liquid mass flow rate and high gas mass
345 flow rate, for the nozzle with shorter mixing port, there is not enough time for the wavy structure to be
346 formed in liquid core/film; thus the liquid and gas do not align while co-flowing. Hence, gas impinges at
347 an angle on the liquid sheets outside the nozzle, leading to vigorous break up of liquid sheets into small
348 fragments; this process was termed as Prompt Atomization. If one observe carefully the data points for
349 nozzles F and G in the Figure 2, it can be seen that for the small values of GLR (say $GLR < 3$) there is not
350 much difference between P_m/P_a ratio for the nozzle with long mixing port (nozzle G) and the nozzle
351 with short mixing port (nozzle F). For the values of $GLR \geq 3$ this difference increases. Smaller values of
352 GLR mean lower gas mass flow rate or relatively higher liquid flow rate and large value of GLR means
353 vice versa. This difference in pressure drop coincides with the performance of the nozzles as observed
354 by Song and Lee (Song & Lee, 1996). Finally, comparing the data points of the nozzle A, B and C, it is
355 evident from the plot in Figure 2 that d_m/d_g ratio has the most significant effect on the mixing point
356 pressure among all the geometrical parameters studied. The higher the value of d_m/d_g ratio, the higher
357 is the value of the pressure reduction between the gas inlet pressure and mixing point pressure (nozzle
358 C). Particularly in the range $0.01 < ALR < 0.4$, the influence of d_m/d_g is more significant, indicating that
359 the gas pressure drop in this range is more when the d_m/d_g ratio is incremented. Similarly, P_w/P_a has
360 the same behavior as function of GLR as that of P_m/P_a for the geometrical parameters studied (Figure
361 5).



362

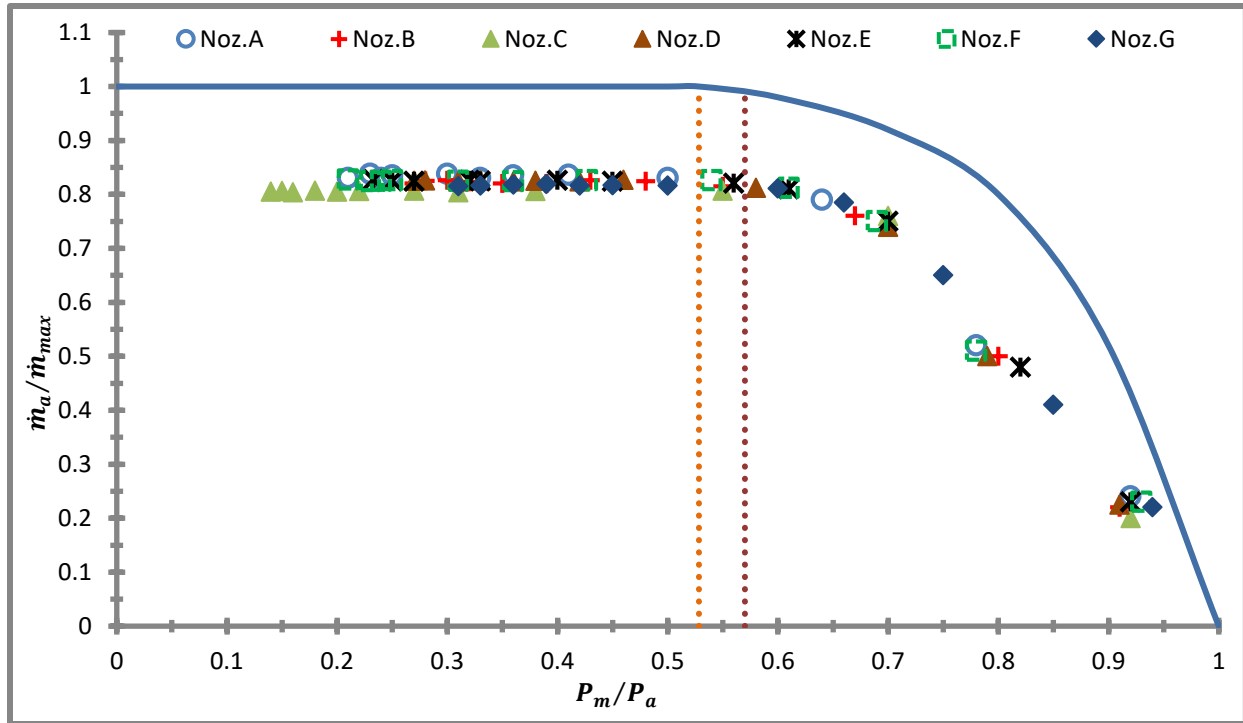
363 **Figure 4:** Plot of mixing point pressure to air inlet pressure ratio against gas to liquid mass flow rate ratio.

364



365

366 **Figure 5:** Plot of water inlet pressure to air inlet pressure ratio against gas to liquid mass flow rate ratio.



367

368 **Figure 6:** Plot of the ratio of air mass flow rate to maximum air mass flow rate through gas port against pressure ratio. The
 369 continuous blue line is the curve for isentropic flow through converging-diverging nozzle.

370 Figure 6 depicts the ratio of air mass flow rate to the maximum air mass flow rate (for $Ma=1$ at the
 371 throat between gas port and mixing port) as a function of pressure ratio (P_m/P_a). In the same figure, the
 372 curve for isentropic flow through converging-diverging nozzle is also plotted (continuous line). The flow
 373 in Y-jet atomizers from gas port to the mixing port is similar to the flow through converging diverging
 374 nozzle where d_g act as a nozzle throat and P_m (mixing point pressure) as the back pressure. The
 375 deviation of the data points from the isentropic prediction line is due to the irreversibility of the sudden
 376 expansion of the air and the presence of liquid around the mixing point. This behavior is also observed
 377 by Ferreira et al (Ferreira, et al., 2009) . The orange dashed line shows the pressure ratio ($P_m/P_a =$
 378 0.5283) at which isentropic compressible flow through a converging-diverging nozzle is choked. The red
 379 dashed line ($P_m/P_a = 0.565$) shows the deviation of the shocked region from the isentropic
 380 compressible flow. Ferreira et al (Ferreira, et al., 2009) explained that presence of the water in the
 381 mixing port restricts the air flow; the liquid mass flow rate changes the value of gas mass flow rate at
 382 which flow is choked for the same geometric expansion (d_m/d_g). However, the choked condition
 383 always occurs at the exit of the gas-port not down stream of this point (Pacifico & Yanagihara, 2014) &
 384 (Ferreira, et al., 2009). Ferreira et al (Ferreira, et al., 2009) observed that smallest SMD (Saunter Mean
 385 Diameter) are produced at choked conditions. This is an important operational parameter for internally

386 mixing twin-fluid atomizers. However, in the case of thermal power plants, when operating at choked
 387 conditions, large amount of steam flow at high velocity is supplied to the combustion chamber. The
 388 intense interaction with the turbulence field induces high strain rates in the flame front leading to local
 389 flame extinction; this elongation of the flame might end up in a contact with boiler wall. In these cases,
 390 the reaction times become larger than the mixing time, leading to formation of soot (Warnatz, et al.,
 391 2001). Secondly, large amount of water introduced into the flame cools down the reaction zone leading
 392 to decrease in local temperature that might lead to flame extinction and prevent re-ignition of the
 393 mixture.

394 In order to compare all the parameters analyzed in Figure 4 and Figure 5 with the empirical correlations
 395 for P_m/P_a and P_w/P_a proposed by Pacifico & Yanagihara (Pacifico & Yanagihara, 2014), data points of all
 396 the nozzles A-G and the correlations of P_m/P_a and P_w/P_a are plotted in Figure 7 and Figure 8
 397 respectively. The correlations are:

$$\frac{P_m}{P_a} = 0.169 + 0.81 \exp \left[-0.675 \theta^{-0.22} \left(\frac{l_m}{d_m} \right)^{-0.38} \left(\frac{d_m}{d_g} \right)^4 GLR^{0.87} \right] \quad (13)$$

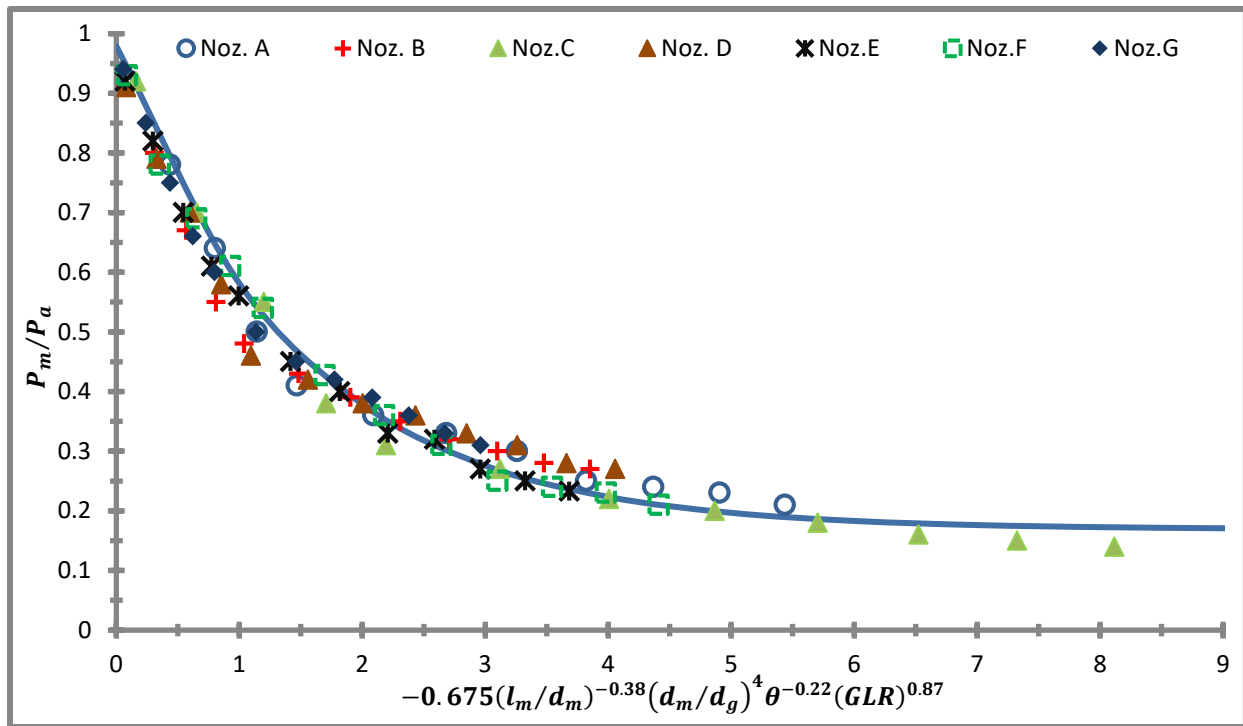
$$\frac{P_w}{P_a} = 0.161 + 1.06 \exp \left[-1.08 \theta^{-0.11} \left(\frac{l_m}{d_m} \right)^{-0.25} \left(\frac{d_m}{d_g} \right)^3 GLR^{0.82} \right] \quad (14)$$

398
 399 These correlations, shown in Eq. 13 and Eq. 14, are valid for the range $0 \leq GLR \leq 1$; $3.5 \leq l_m/d_m \leq 10$;
 400 $1.67 \leq d_m/d_g \leq 2$; and $45^\circ < \theta < 70^\circ$. In these correlations, θ must be in radians ($\pi/4 < \theta < 7\pi/18$).
 401 It can be seen in the Figures 7 & 8 that there is a good agreement between the proposed correlations
 402 and the current simulation results. An important operational parameter is the condition of critical gas
 403 flow. For the present numerical study it is $P_m/P_a < 0.565$; this is obtained when
 404 $-0.675 \theta^{-0.22} (l_m/d_m)^{-0.38} (d_m/d_g)^4 GLR^{0.87} > 1.05$.

405 Figure 9 shows the plot of the data points obtained from the simulations and the plot of the correlation
 406 ($P(z)/P_a$) proposed by Pacifico & Yanagihara (Pacifico & Yanagihara, 2014) for the pressure drop along
 407 the length of the mixing chamber. Numerical results agree well with the proposed correlation.
 408 Following is the correlation:

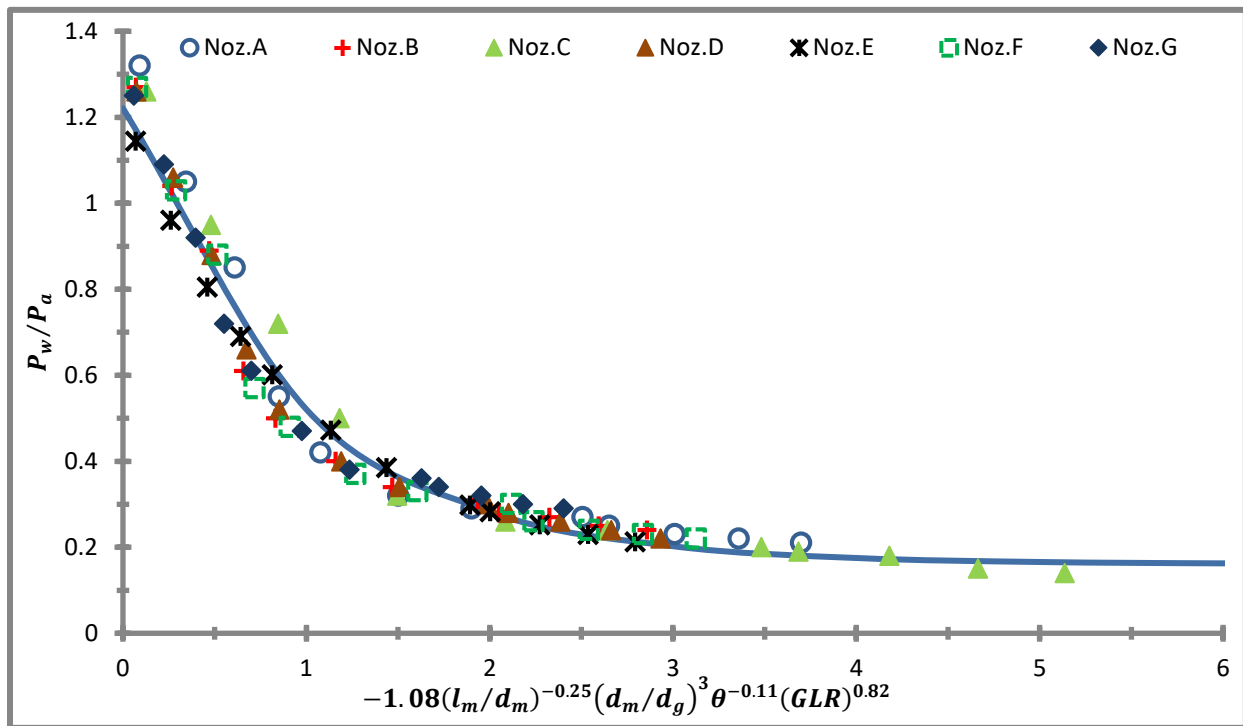
$$\frac{P(z)}{P_a} = 0.172 + 0.732 \exp \left[-0.371 \theta^{-0.203} \left(\frac{l_m}{d_m} \right)^{-0.422} \left(\frac{d_m}{d_g} \right)^{5.152} GLR^{0.988} - 1.286 \left(\frac{z}{l_m} \right)^{1.251} \right] \quad (15)$$

409



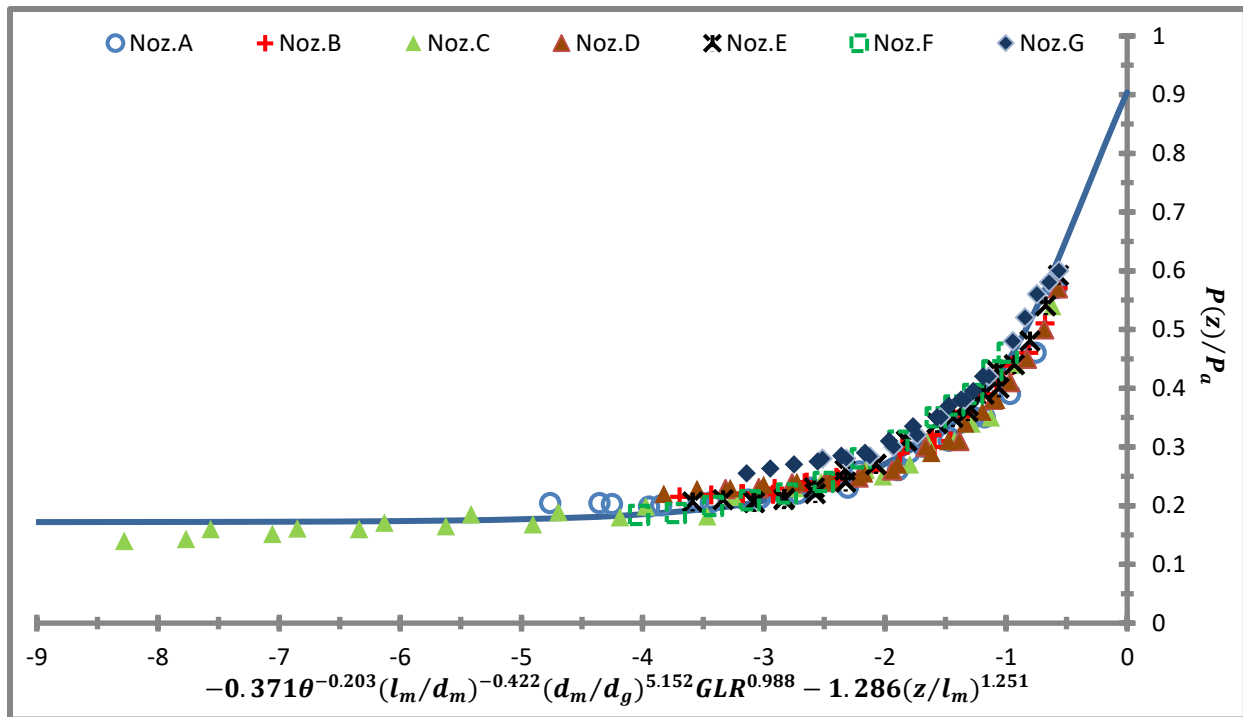
410

411 **Figure 7:** Comparison of numerical data points against empirical correlation (Eq. 13) for the mixing point pressure to the air
 412 inlet pressure ratio proposed by Pacifico & Yanagihara (Pacifico & Yanagihara, 2014).



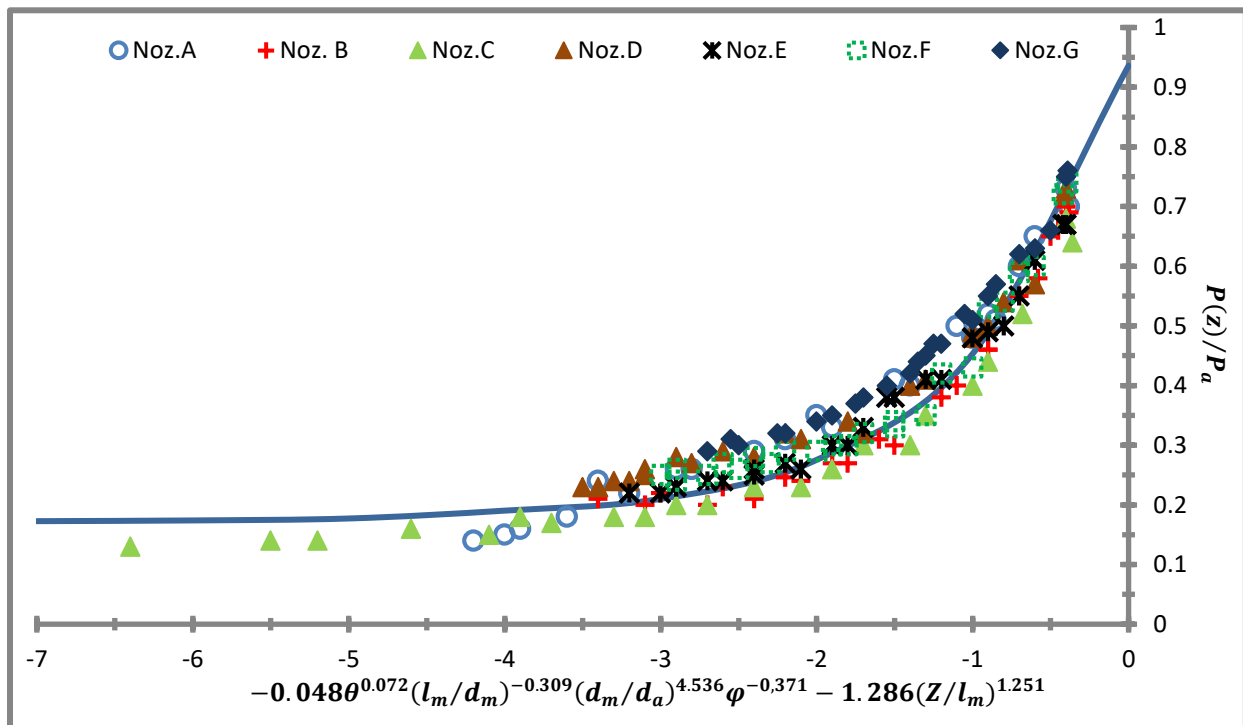
413

414 **Figure 8:** Comparison of numerical data points against empirical correlation (eq. 14) for the water inlet pressure to the air
 415 inlet pressure ratio proposed by Pacifico & Yanagihara (Pacifico & Yanagihara, 2014).



416

417 **Figure 9:** Comparison of numerical data points against the empirical correlation (eq. 15) based on GLR for the pressure drop
 418 along the length of the mixing port proposed by Pacifico & Yanagihara (Pacifico & Yanagihara, 2014).



419

420 **Figure 10:** Comparison of numerical data points against the empirical correlation (eq. 17) based on momentum ratio (ϕ) for
 421 the pressure drop along the length of the mixing port proposed by Pacifico & Yanagihara (Pacifico & Yanagihara, 2014).

422 Another parameter used for the analysis of internally mixing twin-fluid Y-jet atomizer is the ‘Momentum
 423 Ratio’ (φ); this is the ratio of the momentum of the liquid jet going into the mixing port and momentum
 424 of the auxiliary fluid (air or steam). This ratio was first used by (Michhele, et al., 1991) for the analysis of
 425 twin-fluid Y-jet atomizers. It is used in previous studies by (Song & Lee, 1996), (Andreussi, et al., 1992),
 426 (Mlkvik, et al., 2015) and (Nazeer, et al., 2018). Momentum ratio is defined as:

$$\varphi = \frac{G_l^2 d_l^2 \rho_{a,m} \sin\theta}{G_{g,m}^2 d_m^2 \rho_w} \quad (16)$$

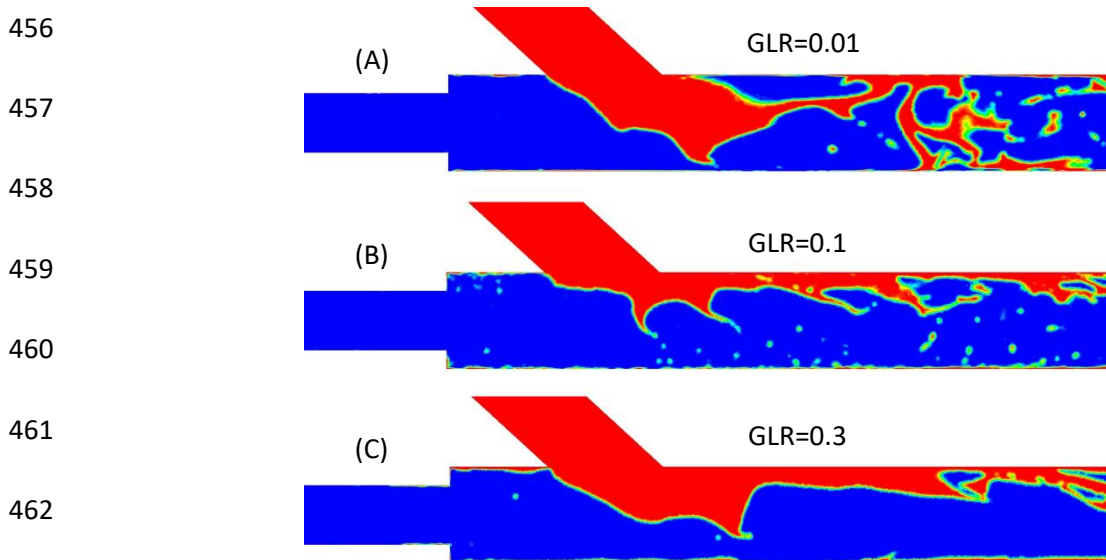
427
 428 Where G_l is the liquid mass velocity, $G_{g,m}$ is the gas mass velocity based on mixing port cross sectional
 429 area, $\rho_{a,m}$ is the gas density at the mixing point.

430 The correlation based on momentum ratio for the pressure drop along the length of the mixing chamber
 431 ($P(z)/P_a$) proposed by pacific & Yanagihara is plotted in Figure 10. Numerical data points are also
 432 plotted on the same figure. Again the results agree well with the proposed correlation. Following is the
 433 correlation:

$$\frac{P(z)}{P_a} = 0.172 + 0.764 \exp \left[-0.048 \theta^{0.072} \left(\frac{l_m}{d_m} \right)^{-0.309} \left(\frac{d_m}{d_a} \right)^{4.536} \varphi^{-0.371} - 1.286 \left(\frac{z}{l_m} \right)^{1.251} \right] \quad (17)$$

434
 435 Figure 11 shows the contours of the volume fraction for nozzle ‘D,’ for the three different GLR ratios.
 436 When the GLR ratio is low (0.01; Figure 11a), the flow seems to be somewhat transitional between
 437 froth/churn-turbulent flow and annular-wispy flow. As the GLR increases (0.1, Figure 11b) the flow is
 438 clearly in the wispy-annular regime with an annular liquid film surrounding the gas core comprising of
 439 dispersed droplets and ligaments. As the GLR increases further (0.3, Figure 11c), the flow is clearly in the
 440 annular flow regime, with a wavy annular film around and gaseous core. These changes in the flow
 441 patterns occurring upstream of the discharge orifice greatly affect the atomization and spray formation
 442 downstream of the nozzle exit. For instance, when the flow within the nozzle is churn-turbulent flow,
 443 the spray formed is not stable; whilst, if the flow pattern is annular, the nozzle operates as plain-jet air-
 444 blast atomizer, comprising a central core of high velocity gas surrounded by annular film of liquid. The
 445 relative velocity between the gas and liquid ensure good atomization.

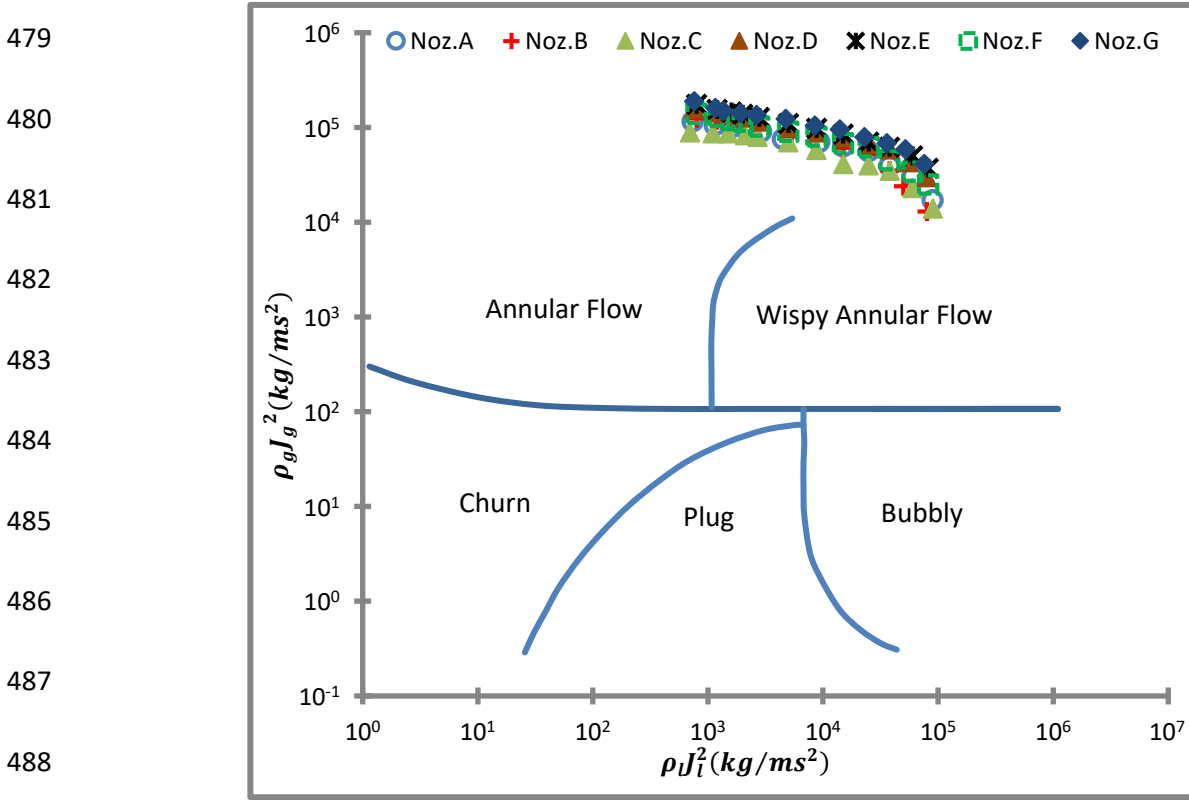
446 In order to verify the flow regimes, the data points of all the nozzles were plotted on the vertical pipe
447 flow regime map proposed by (Hewitt & Roberts, 1969) and (Oshinnowo & Charles, 1974). There are of
448 course, some significant differences between the 'classical' flow regimes examined in literature and the
449 types of flow patterns that can arise in practical atomizers. The former is confined to fully developed
450 flow in long constant cross-section pipes; whereas the flow in the atomizer is of short length and the
451 flow is transient in nature, roughly equivalent to the flow at the inlet of the long pipes. Moreover, the
452 flow in the atomizer is accelerating from the mixing duct to the exit orifice. However, despite these
453 aforementioned differences in the flow nature, the flow patterns that are normally associated with the
454 two-phase flow in long pipes can usefully contribute to the better understanding of the flow regimes in
455 the atomizers (Chin & Lefebvre, 1993).



463 **Figure 11:** Contour of volume fraction of air-water multiphase flow at three different
464 **GLRs.**

465 Figure 12 shows the Hewitt and Robert's multiphase flow map (Hewitt & Roberts, 1969). This map has
466 been found to fit a reasonably large range of fluids and is of particular interest in the high mass flux
467 region (Hawkes, et al., 2000). The coordinates represent the momentum fluxes; the ordinate represents
468 the air momentum flux while abscissa represents water momentum flux. J_w and J_a are superficial
469 velocities of water and air respectively. The data points for all seven nozzles are also plotted on this map.
470 It can be seen that the main flow patterns are annular and wispy annular. GLR ratio decreases with
471 increase in water momentum flux; then according to this map, for small values of GLR, the wispy annular
472 is the main flow pattern while for larger values of GLR, the annular flow is the main flow pattern. This
473 result matches with the flow pattern observed within the nozzle (Figure 11 b & c). However, there is

474 small discrepancy between the results, at the lowest value of GLR in the study (0.01) flow seems to be
 475 transitional between the froth/churn turbulent flow and the wispy annular flow (Figure 11 a), while,
 476 according to the map, it should be wispy-annular flow. Nevertheless, in industrial boilers the GLR ratio is
 477 usually between $0.1 < \text{GLR} < 0.3$. Flow is wispy annular at the lower end of this range and annular at
 478 the higher end of the range.



489 **Figure 12: Data points plotted on vertical multiphase pipe flow regime map of (Hewitt & Roberts, 1969).**

490 Figure 13 shows the flow pattern map provided by (Oshinnowo & Charles, 1974) for the vertical
 491 downward flow. In this figure, the ordinate is the square root of the air-liquid volumetric flow rate ratio,
 492 while the abscissa is the ratio of the two-phase Froude Number, Fr_{tp} , to the square root of A where,

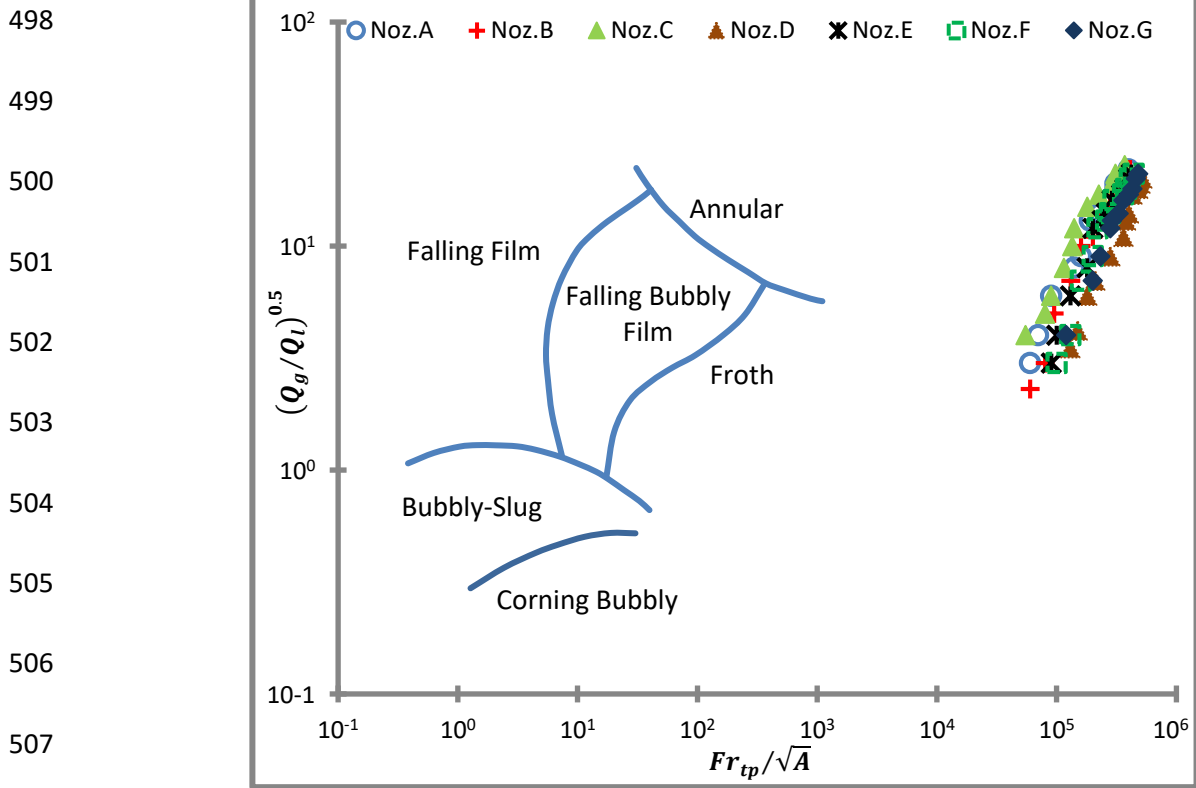
$$Fr_{tp} = \frac{U_s^2}{gd_m} \quad (18)$$

$$A = \frac{\mu_l'}{(\rho_l' \sigma'^3)^{0.25}} \quad (19)$$

493 and J , the superficial velocity of the two phase flow is obtained as

$$J = \frac{Q_a + Q_l}{(\pi/4)d_m^2} \quad (20)$$

494 It can be clearly seen that the results lie outside the flow regime established by the map. Nevertheless,
 495 one could easily speculate from the map that for the very low GLRs used in the study, the flow has to be
 496 froth or transition between froth and annular flow, while for higher values of GLR, the flow has to be
 497 annular; this result matches with the contours displayed in the Figure 11.



508 **Figure 13:** Data points plotted on vertical multiphase pipe flow regime map of (Oshinnowo & Charles, 1974).

509 **Conclusion**

510 A parametric analysis to study the effect of operational and geometric parameters on the internal flow
 511 characteristics of twin-fluid Y-Jet atomizer has been carried out; seven atomizers with different
 512 geometrical parameters have been considered. Moreover, 11 cases for each atomizer with different GLR
 513 (gas to liquid mass flow rate) ratios have been simulated, giving a total of 77 cases. The working fluids
 514 were water and air. The compressible Navier-Stokes equation were used to model the flow through the
 515 atomizer, utilizing their implementation into ANSYS FLUENT. Hybrid RANS and LES technique i.e. WMLES
 516 (wall modeled large eddy simulations) was used to resolve the larger eddies with LES simulation, while
 517 smaller eddies near the wall were modeled with the Prandtl Length Model. The volume of fluid method
 518 was used to capture the development and fragmentation of the gas liquid-interface inside Y-jet atomizer.

519 The results show that gas–liquid multiphase regime formed is annular flow for the vast majority of GLR
520 ratios. The sudden expansion of gas jet from gas-port into the mixing duct is limited by higher pressure
521 of the liquid jet emanating from liquid port; this leads to recirculation of the air in the premixed zone of
522 the nozzle, which, in turn, results to reverse film formation in the premixed zone. The numerical results
523 obtained have been compared with empirical correlations of the pressure drop for twin-fluid Y-jet
524 atomizer available in open literature and have been found to agree well with them. These correlations
525 could be used for designing Y-jet atomizer, and predicting the occurrence of critical conditions at the
526 exit of the gas port. Moreover, the results show that the mixing point pressure is strongly dependent on
527 the mixing port to airport diameter ratio, specifically in the range $0.1 < (GLR) < 0.4$; the mixing port
528 length moderately affects the mixing point pressure while the angle between mixing and liquid ports
529 was found not to have an appreciable effect. Despite some significant difference between the
530 multiphase flow in pipes and the flow that could arise in the Y-jet atomizers, the classical pipe
531 multiphase flow regime maps could be applied to the flow through the mixing duct of twin-fluid Y-jet
532 atomizers. The main flow regimes found under the studied operational conditions are annular and wispy
533 annular flow.

534

535 **Acknowledgement**

536 The project has received funding from European Union Horizon-2020 Research and Innovation MSCA-
537 ITN Programme with acronym HAOS: Grant Agreement No. 675676.

538 **Appendix A: Speed of Sound in Gas-Liquid Mixture**

539 Consider a unit infinitesimal mixture of disperse phase (liquid) and continuous phase (gas). The initial
540 densities are denoted by ρ_l and ρ_g and initial pressure in continuous phase by P_g . Surface tension, σ , can
541 be included by denoting the radius of the dispersed phase particle by R . Then the initial pressure in the
542 dispersed phase is $P_l = P_g + 2\sigma/R$.

543 Now consider an infinitesimal change in pressure P_l to $P_l + \delta P_l$. Any dynamics associated with the
544 resulting fluid motion is ignored. It is assumed that new equilibrium state is achieved. In the absence of
545 any mass exchange between the phases, the new dispersed and continuous phase volumes are
546 respectively

547

$$(\rho_l \alpha_l) / \left[\rho_l + \frac{\partial \rho_l}{\partial P_l} \Big|_s \delta P_l \right] \quad (21)$$

$$(\rho_g \alpha_g) / \left[\rho_g + \frac{\partial \rho_g}{\partial P_g} \Big|_s \delta P_g \right] \quad (22)$$

548 Adding these together and subtracting from unity, one obtains change in the total volume, δV , and
 549 hence sonic velocity c as

$$\frac{1}{c^2} = -\rho \frac{\delta V}{\delta P_g} \Big|_{\delta P_g \rightarrow 0} \quad (23)$$

$$\frac{1}{\rho c^2} = \frac{\alpha_l \partial \rho_l}{\rho_l \partial P_l} \Big|_s \frac{\delta P_l}{\delta P_g} + \frac{\alpha_g \partial \rho_g}{\rho_g \partial P_g} \Big|_s \quad (24)$$

550 If we assume that no dispersed phase particles are created or destroyed, then the ratio $\delta P_l / \delta P_g$ could be
 551 determined by evaluating the new dispersed particle size $R + \delta R$ commensurate with the new disperse
 552 phase volume and using the relation $\delta P_l = \delta P_g - \frac{2\sigma}{R^2} \delta R$:

$$\frac{\delta P_l}{\delta P_g} = \left[1 / \left(1 - \frac{2\sigma}{3\rho_l R} \frac{\partial \rho_l}{\partial P_l} \Big|_s \right) \right] \quad (25)$$

553 Substituting this into the equation 24 and using, the notations

$$\frac{1}{c_l^2} = \frac{\partial \rho_l}{\partial P_l} \Big|_s ; \quad \frac{1}{c_g^2} = \frac{\partial \rho_g}{\partial P_g} \Big|_s \quad (26)$$

554 the result could be expressed as

$$\frac{1}{\rho c^2} = \frac{\alpha_g}{\rho_g c_g^2} + \frac{\alpha_l / \rho_l c_l^2}{[1 - 2\sigma / 3\rho_l c_l^2 R]} \quad (27)$$

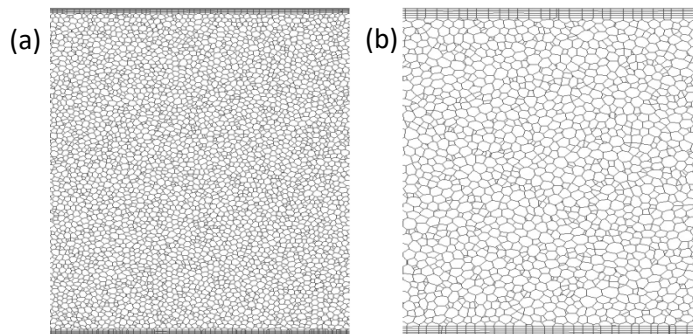
555 For the sake of simplification and in most of practical circumstances the surface tension effect can be
 556 neglected since $\sigma \ll \rho_l c_l^2 R$, then eq. 27 could be expressed as

$$\frac{1}{\rho c^2} = \frac{\alpha_g}{\rho_g c_g^2} + \frac{\alpha_l}{\rho_l c_l^2} \quad (28)$$

557 ρc^2 is the effective bulk modulus of the mixture where the effective density $\rho = \alpha_g \rho_g + \alpha_l \rho_l$ is
 558 governed by the density of the liquid and the inverse of effective bulk modulus is equal to an average of
 559 the inverse bulk moduli of the components ($1/\rho_g c_g^2$ and $1/\rho_l c_l^2$) weighted according to their volume
 560 fractions.

561 **Appendix B: Grid Independent Study**

562 A grid independence study was conducted to check whether flow regimes changes with the grid. Figure
563 14 a shows the grid used in the parametric study for nozzle D and Figure 14 b shows the coarser grid.
564 Grid 'a' has about 17 million elements and grid 'b' has around 13 million elements. The total number of
565 elements around the circumference of the mixing duct for the grid 'a' are 390 while for grid 'b' are 280.
566 The Y^+ value for the grid 'a' is 0.72 while for grid 'b' is 0.92.



572 **Figure 14: (a) grid used in the parametric study, (b) coarser grid.**

573 Figure 15 shows contours of average volume fraction of water over one hundred thousand time steps.
574 The time step size is 1×10^{-8} s. Figure 15 a & b depicts the average volume fraction for froth/churn-
575 turbulent flow regime (GLR=0.01), Figure 15 c & d depicts the average volume fraction for wispy-annular
576 flow regime (GLR=0.1) and Figure 15 e & f depicts the average volume fraction of annular flow regime
577 (GLR=0.3). The average volume fraction of all the three flow regimes is almost the same for coarser and
578 dense grid.

579

580

581

582

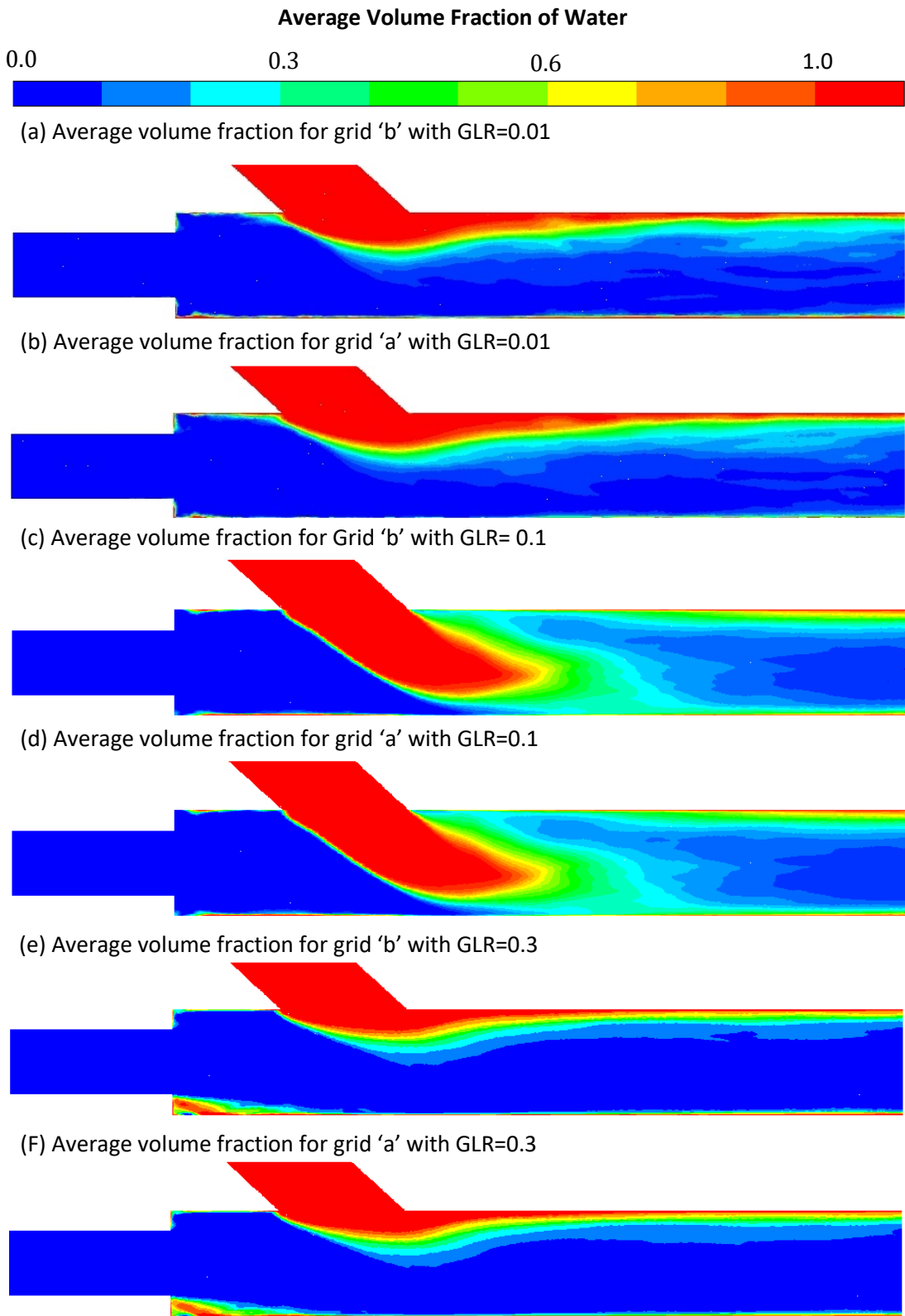
583

584

585

586

587
588
589
590
591
592
593
594
595
596
597
598
599
600
601
602
603
604
605
606
607
608



609

Figure 15: Average volume fraction of water over one hundred thousand time steps (a & b) average volume fraction for froth/churn-turbulent flow regime, (c & d) average volume fraction for wispy-annular flow regime and (e & f) average volume fraction for annular flow regime.

610 **References**

- 611 Andreussi, P. et al., Measurement of Film Thickness within a Y-Jet Atomizer, *International conference on*
612 *liquid atomization and spray systems*, Rouen, France, pp. 632-639, 1994.
- 613 Andreussi, P., Tognotti, L., Michele, G. D. & Graziadio, M., Design and Characterization of Twin-Fluid Y-
614 Jet Atomizers, *Atomization and Sprays*, Vol. 2, pp. 45-59, 1992.
- 615 Arcoumanis, C. & Gavaises, M., Argueyrolles, B. and Galzin, F. 1999. Modelling of Pressure-Swirl
616 Atomizers for GDI Engines, *SAE Transactions, Journal of Engines, 1999-01-0500*, Vol. 108-3, 1999.
- 617 Arcoumanis, C., Gavaises, M., Abdul-Wahab, E. & V., M., 1999. Modeling of Advanced High-Pressure Fuel
618 Injection Systems for Passenger Car Diesel Engines, *SAE Transactions Journal of Engines, 1999-01-0910*,
619 Vol. 108-3, 1999.
- 620 Barreras, F., Lozano, A., Barroso, J. & Lincheta, E., Experimental characterization of industrial twin-fluid
621 atomizers. *Atomization and Sprays*, Vol. 16, pp. 145-147, 2006.
- 622 Barreras, F., Lozano, A., Ferreira, G. & Lincheta, The effect on the inner flow on the performance of a
623 twin-fluid nozzle with an internal mixing chamber, *Proc. of ILASS-Europe Conference, Como, Italy, 2008*.
- 624 Barreras, F., Lozano, A., Ferreira, G. & Lincheta, E., Study of the Internal Flow Condition on the Behavior
625 of Twin-Fluid Nozzle with Internal Mixing Chamber, *ICLASS, Kyoto, Japan, 2006*.
- 626 Brackbill, J. U., Kothe, D. B. & Zemach, C., A continuum method for modeling surface tension. *Journal of*
627 *Computational Physics*, vol. 100-3, pp. 335-354, 1992..
- 628 Bryce, W., Cox, N. & Joyce, W., Oil droplet production and size measurement from a twin-fluid atomizer
629 using real fluids, *3rd International Conference on Liquid Atomization and Sprays*, pp. 259-263, Tokyo,
630 Japan, 1978.
- 631 Chin, J. S. & Lefebvre, A. H., Flow Patterns in Internal-Mixing Twin-Fluid Atomizers, *Atomization and*
632 *Sprays*, Vol. 3, pp. 463-374, 1993.
- 633 Crowe, C., *Multiphaseflow handbook*, Newyork: Taylor & Franks, 2006.
- 634 Dafsari, R. A., Vashali, F., Lrr, J., Effect of swirl chamber length on the atomization characteristics of a
635 pressure swirl nozzle, *Atomization and Sprays*, Vol. 27-10, pp. 859-874, 2017.
- 636 Dombrowski, N., Hanson, D. & Ward, D., Some Aspects of Liquid Flow Through Fan Spray Nozzles.
637 *Chemical Engineering Science*, Vol. 12, pp. 33-50, 1960.
- 638 Dombrowski, N. & Johns, W., The aerodynamic instability and disintegration of viscous liquid sheets,
639 *Chemical Engineering Science*, Vol. 8-7, pp. 203-214, 1963.

640 El-Batsh, H.M., D. M. & Hassan, A., On the application of mixture model for two-phase flow induced
641 corrosion in a complex pipeline configuration, *Applied Mathematical Modeling*, Vol. 36, pp. 5686-569,
642 2002.

643 Esfarjani, S. A. & Dolatabadi, A., 3D simulation of two-phase flow in an effervescent atomizer for
644 suspension plasma spray, *Surface Coating Technology*, Vol. 203, pp. 2074-2280, 2009.

645 Ferreira, G., Barreras, F., Lozano, A., Garcia, J. A., Lincheta, E., Effect of inner two –phase flow on the
646 performance of an industrial twin-fluid nozzle with an internal mixing chamber, *Atomization and Sprays*,
647 Vol. 19, pp. 873-884, 2009.

648 Ferreria, G., Garcia, J. A., Barreras, F., Lozano, A., & Lincheta, E., Design and optimization of twin-fluid
649 atomizers with an internal mixing chamber for heavy fuel oils, *Fuel Processing Technology*, Vol. 90, pp.
650 270-278, 2009.

651 Gadgil, H. P. & Raghunandan, B. N., Some features of spray breakup in effervescent atomizers,
652 *Experiments in Fluids*, Vol. 50, pp. 329-338, 2011.

653 Gopala, V. R. & Berend, G. M., Volume of Fluids Methods for Immiscible-Fluids and Free-Surface Flows,
654 *Chemical Engineering Journal*, Vol. 141, pp. 204-221, 2008.

655 Hawkes, N., Lawrence, C. & Hewitt, G., Studies of Wispy-Annular Flow Using Transient Pressure Gradient
656 and Optical Measurement, *International Journal of Multiphase Flow*, Vol. 26, pp. 1565-1582, 2000.

657 Hewitt, G. F. & Roberts, D.N., Studies of two-phase flow patterns by simultaneous X-ray and flash
658 photography, Harwell, UK, Tech. Rep. AERE-M2159, February, 1969.

659 Hinze, J. O., *Turbulence*, New York: McGraw-Hill Publishing Co, 1975.

660 Naseri, H., Trickett, K., Mitroglou, N., Karathanassis, I., Koukouvinis, P., Gavaises, M., Barbour, R.,
661 Santini, M., Wang, J., Turbulence and Cavitation Suppression by Quaternary Ammonium Salt Additives,
662 *Nature Scientific Reports* 8, Article number: 7636, 2018.

663 Huang, X., Wang, X. & Liao, G., Characterization of an effervescent atomization water mist nozzle and its
664 fire suppression tests, *Proceedings of Combustion Institute*, pp. 2573-2579, 2011.

665 Jang, X., Siamas, G. A., Jagus, K. & Karayiannis, T., Physical Modelling and Advanced Simulations of Gas-
666 Liquid two-phase jet flows in atomization and sprays, *Progress in Energy and Combustion Science*, Vol.
667 36, pp. 131-167, 2010.

668 Kieffer, S. W., Sound Speed in Liquid-Gas Mixtures: Water-Air and Water-Steam, *Journal of Geophysical*
669 *Research*, Vol 82, pp. 2895-2904, 1977.

670 Koukouvinis, P., Gavaises, M., Li, J. & Wang, L., Large Eddy Simulation of Diesel Injector Including
671 Cavitation Effects and Correlation to Erosion Damage. *Fuel*, Vol. 175, pp. 26-3, 2016.

672 Koukouvinis, P., Naseri, H., and Gavaises, M., Performance of Turbulence Models and Effect of Cavitation Models in
673 Prediction of Incipient Cavitation, *International Journal of Engine Research*, 2016

674 Lakhehal, D., Meier, M. & Fulgosi, M., Interface Tracking towards the Direct Simulation of Heat and Mass
675 Transfer in Multiphase Flows, *International Journal of Heat and Fluid Flow*, Vol. 23, pp. 242-257, 2002.

676 Lang, R., Ultrasonic Atomization of Liquids, *Journal of Acoustical Society of America*, Vol. 34-1, pp. 6-8,
677 1962.

678 Lefebvre, A. H., Twin-Fluid Atomization: Factors Influencing Mean Drop Size, *Atomization and Sprays*,
679 Vol. 2, pp. 101-119, 1992.

680 Lefebvre, A. H., A Novel Method of Atomization with Potential Gas Turbine Application. *Defense Sci. J.*,
681 Vol. 38, pp. 353-362, 1988.

682 Li, S., Yang, X. Y., Fu, C., Li, T. Y. and Gao, Y., Experimental Investigation of near-field breakup
683 characteristics of hybrid-mix twin-fluid atomizers, *Atomization and Sprays*, Vol. 28-10, pp. 901-914, 2018.

684 Li, Z., Wua, Y., Cai, C., Zhang, H., Gong, Y., Takeno, K., Hashiguchi, K., & Lu, J., Mixing and atomization
685 characteristics in an internal-mixing twin-fluid atomizer. *Fuel*, Volume 97, pp. 306-314, 2012.

686 Loebker, D. & Empie, H. J., High mass flowrate effervescent spraying of high viscosity Newtonian liquid,
687 Ottawa, *10th Annual Conference on Liquid Atomization and Spray Systems*, Ottawa, Japan, pp. 253–257,
688 1997.

689 Loth, E., *Computational Fluid Dynamics of Bubbles, Drops and Particles*. Cambridge: Cambridge
690 University Press, 2009.

691 Maski, D. & Durairaj, D., Effects of electrode voltage, liquid flow rate, and liquid properties on spray
692 chargeability of an air-assisted electrostatic-induction spray., *Journal of Electrostatics*, vol. 68-2, pp. 152-
693 158, 2010.

694 McWilliam, D. & Duggins, R., Speed of Sound in Bubbly Liquids, *Proceedings of the Institution of*
695 *Mechanical Engineering* Vol. 184-3, pp. 102-107, 1969.

696 Michhele, D. G., Graziadio, M., Morelli & Novelli, G., Characterization of the Spray Structure of a Large
697 Scale H.F.O. Atomizer, Gaithersburg, *Proceedings of ICLASS*, Gaithersburg, USA, vol. 99, pp. 779-
698 786, 1991.

699 Mitroglou, N. & Gavaises, M., Cavitation Inside Real-Size Fully Transparent Fuel Injector Nozzles and Its
700 Effect on Near-Nozzle Spray Formation, *Proceedings of Workshop on Droplet Impact Phenomena and*
701 *Spray Investigations (DIPSI)*, University of Bergamo, Italy, 2011.

702 Milkvik, M., Stahle, P., Shuchmann, H.P., Gaukel, V., Jedelsky, J., and Jicha, M., Twin-Fluid atomization of
703 viscous liquids: The Effect of atomizer construction on breakup process, spray stability and droplet size.
704 *International Journal of Multiphase*, Vol. 77, pp. 19-31, 2015.

705 Mujumdar, A. S., Huang, L. X. & Chen, X. D., An overview of the recent advances in spray-drying.. *Dairy*
706 *Sci. Technolgy*, Vol. 90, pp. 211-224, 2010.

707 Mullinger, P. & Chigier, N., The Design and Performance of Internal Mixing Multijet Twin Fluid Atomizers,
708 *Journal of the institute fuel*, Vol. 47, pp. 251-261, 1974.

709 Nazeer, Y., Ehmann, M., Koukouvinis, F. & Gavaises, M., Internal Flow Characteristics of Twin-Fluid 'Y'
710 Type Internally Mixing Atomizer, *Proceedings of ICLASS*, Chicago, USA, 2018.

711 Nguyen, D. & Rhodes, M. J., Producing Fine Drops of Water by Twin-Fluid Atomization, *Powder*
712 *Technology*, Vol. 99, pp. 285-292, 1998.

713 Oshinnowo, T. & Charles, M. E., Vertical Two-Phase Flow; Part1, Flow Pattern Correlations. *Journal of*
714 *Chemical Engineering*, Vol, 52, pp. 25-35, 1974.

715 Pacifico, A. L. & Yanagihara, J. I., The influence of geometrical and operational parametrs on Y-jet
716 atomizers performance, *Journal of Brazilian Society of Mechanical Science and Engineering*, Vol. 36, pp.
717 13-32, 2014.

718 Piomelli, U. & Balaras, E., Wall-layer Models for Large-Eddy Simulations. *Annual Review of Fluid*
719 *Mechanics* , Vol. 34, pp. 349-374, 2002.

720 Prasad, K. S. L., Characterization of Air Blast Atomizers, *Proceedings of ICLASS*, Wisconsin, USA, 1982..

721 Radcliffe, A., The performance of a Type of Swirl Atomizer, *Proceedings of the Institution of Mechanical*
722 *Engineers*, Vol. 169, pp. 93-106, 1955.

723 Saleh, A., Amini, G., & Dolatabadi, A., Penetration of Aerated Suspension on Spray in a Gaseous
724 Crossflow, *Atomization and Sprays*, vol. 28-2, pp. 91-110, 2018.

725 Shur, M. L., Spalart, P. R., Strelets, M. K. & Travin, A. K., A hybrid RANS-LES approach with delayed-DES
726 and wall-modelled LES capabilities *International Journal of Heat and Fluid Flow*, Vol. 29, pp. 1638-1649,
727 2008.

728 Shur, M., Strelets, P., Spalart, M. & Travin, A., Detached-eddy simulation of an airfoil at high angle of
729 attack, *Engineering Turbulence Modeling and Measurements*, Vol. 4, pp. 669-678, 1999.

730 Smagorinsky, J., General Circulation Experiments with the Primitive Equations, *Monthly Weather Review*,
731 Vol. 91, pp. 99-16, 1963.

732 Song, S. H. & Lee, S. Y., Study of Atomization Mechanism of Gas/Liquid Mixtures Flowing Through Y-Jet
733 Atomizers, *Atomization and Sprays*, Vol. 6, pp. 193-209, 1996.

734 Song, S. & Lee, S., An Examination of Spraying Performance of Y-Jet Atomizers- Effect of Mixing Port
735 Length. Rouen, *Proceedings of ICLASS*, Rouen, France, 1994.

736 Sovani, S., Sojka, P. & Lefebvre, A., Effervescent Atomization, *Progress in Energy and Combustion*
737 *Sciences*, vol. 27-2, pp. 483-521, 2001.

738 Spalart, P. et al., A new version of detached-eddy simulation, resistant to ambiguous grid densities,
739 *Theoretical and Computational Fluid Dynamics* , vol. 20-3, pp. 181-195, 2006.

740 Spalart, P., Jou, W., Strelets, M. & Allmaras, S., Comments on the Feasibility of LES for Wings, and on a
741 hybrid RANS/LES approach. Louisiana , *1st AFOSR International Conference on DNS/LES* , Ruston, USA,
742 1997.

743 Tanasawa, Y., Miyasaka, Y. & Umehara, M., Effect of Shape of Rotating Disks and Cups on Liquids
744 Atomization, Proceedings of ICLASS, Tokyo, Japan, pp. 165-172, 1978.

745 Tanner, F. X., Feigl, K., Karrio, O. & Windhab, E. J., Modeling and Simulation of air-assist atomizers with
746 applications to food spray, *Applied Mathematical Modeling* , Vol. 40, pp. 6121-6133, 2016.

747 Tapia, Z. & Chavez, A., Internal flow in Y-Jet atomizer- numerical study, Proceedings of ICLASS-Europe,
748 Zaragoza, Spain, 2002 .

749 Van Driest, E. R., On Turbulent flow near a wall. *Journal of Aeronautical Sciences*, Vol. 23, pp. 1007-1011,
750 1956.

751 Wade, R. A. et al., Effervescent atomization at injection pressures in the MPa range, *Atomization Sprays*,
752 Vol. 9, pp. 651-667, 1999.

753 Warnatz, J., Mass, U. & Dibble, R. W., *Combustion: Physical and Chemical fundamentals, Modeling and*
754 *Simulation, Experiments*, 3rd. ed. Berlin: Springer-verlag, 2001.

755 Wen, W. & Piomelli, U., Reynolds-averaged and wall-modelled large-eddy simulations of impinging jets
756 with embedded azimuthal vortices, *European Journal of Mechanics-B/Fluids*, Vol. 55, pp. 348-359, 2016.

757 Wigg, L., The effect of scales on fine sprays produced by large airblast atomizer, Pyestock: National gas
758 turbine establishment, 1959.

759 Zhou, Y. et al., Experimental investigation and model improvement on the atomization performance of
760 single hole Y-jet nozzle with high liquid flowrate, *Powder Technology*, Vol. 199, pp. 248–255, 2010.

761

762

763